



MASTER THESIS

Setup and commissioning of an ellipsometer for the investigation of photocathodes of photomultiplier tubes

Supervisor:

Prof. Dr. Alexander Kappes

Second examiner:

Prof. Dr. Christian Weinheimer

A thesis submitted in fulfilment of the requirements for the degree of
Master of Science at Westfälische Wilhelms-Universität Münster

by

Berit Schlüter

AG Kappes
Institute for Nuclear Physics

December 2021

Declaration of Academic Integrity

I hereby confirm that this thesis on “Setup and commissioning of an ellipsometer for the investigation of photocathodes of photomultiplier tubes” is solely my own work and that I have used no sources or aids other than the ones stated. All passages in my thesis for which other sources, including electronic media, have been used, be it direct quotes or content references, have been acknowledged as such and the sources cited.

Signature:

Date:

I agree to have my thesis checked in order to rule out potential similarities with other works and to have my thesis stored in a database for this purpose.

Signature:

Date:

Contents

| | |
|--|------------|
| Declaration of Academic Integrity | iii |
| 1 Introduction | 1 |
| 2 Neutrino astronomy | 3 |
| 2.1 Neutrino properties | 3 |
| 2.1.1 Neutrino interactions | 3 |
| 2.1.2 Cherenkov radiation | 3 |
| 2.2 IceCube Neutrino Observatory | 4 |
| 2.2.1 IceCube Upgrade and IceCube-Gen2 | 5 |
| 2.2.2 Photomultiplier tubes | 6 |
| 3 Ellipsometry | 9 |
| 3.1 Polarization of light | 9 |
| 3.2 Jones vectors and Jones matrices | 10 |
| 3.2.1 Jones vectors | 10 |
| 3.2.2 Jones matrices | 12 |
| 3.3 Stokes formalism | 12 |
| 3.4 Reflection and Transmission | 14 |
| 3.4.1 Reflection at an interface | 14 |
| 3.4.2 Reflection at a three layer system | 17 |
| 3.5 Principle of Ellipsometry | 18 |
| 3.5.1 Null Ellipsometry | 19 |
| 3.5.2 Rotating Analyzer Ellipsometry | 20 |
| 3.6 Rotating Quarter-Wave Plate Stokes Polarimeter | 21 |
| 4 Setup and characterization of the ellipsometer | 23 |
| 4.1 Ellipsometry setup | 23 |
| 4.2 Alignment and cleaning | 24 |
| 4.3 Characterization | 25 |
| 4.3.1 Polarizer and analyzer | 25 |
| 4.3.2 Quarter-wave plate | 27 |
| 4.3.3 Polarization of the laser | 28 |
| 4.3.4 Incident angle | 30 |
| 5 Ellipsometry measurements | 33 |
| 5.1 Samples | 33 |
| 5.2 Null Ellipsometry | 34 |
| 5.2.1 Compact Disc | 35 |
| 5.2.2 Silicone dioxide/ silicone sample | 39 |
| 5.2.3 Bilayer graphene / silicon carbide sample | 41 |
| 5.3 Rotating Analyzer Ellipsometry | 42 |
| 5.3.1 Compact disc | 43 |

| | | |
|----------|---|-----------|
| 5.3.2 | Silicon dioxide/ silicon sample | 45 |
| 5.3.3 | Bilayer graphene / silicon carbide sample | 47 |
| 6 | Summary and outlook | 49 |
| 7 | Appendix | 51 |
| 7.1 | Laser intensity | 51 |
| 7.2 | Laser power density spectrum | 51 |
| 7.3 | Dielectric function and refractive index | 52 |
| | Bibliography | 57 |

1 Introduction

In recent decades astroparticle physics, especially neutrino physics, has gained significantly more interest because neutrinos, due to their tiny interaction cross section and their neutral charge, are an important and promising messenger in astroparticle physics.

Neutrinos were postulated by Pauli in 1930 to preserve the conservation of energy and momentum which was previously assumed to be broken in the beta decay. Since neutrinos rarely interact with their environment, a direct observation is not possible. In 1956 C. L. Cowan and F. Reines succeeded in detecting the electron antineutrino experimentally in a reverse beta decay. Subsequently, muon neutrinos generated and detected in a proton accelerator in 1962 and in 2000, finally, the tau neutrino was measured [1]. However, there are still many open questions about neutrinos such as their exact mass and their precise oscillation properties. Therefore, large neutrino detectors with different types of operation principles have been built with the goal of understanding more about astroparticle physics through the research of neutrinos.

One of those detectors is the IceCube Neutrino Observatory which was installed in Antarctica and became fully operational in 2011. IceCube detects neutrinos indirectly by detecting the Cherenkov light which is produced by secondary charged particles that are produced after a neutrino interaction. The current detection volume is about one cubic kilometer and the detection medium is deep glacial ice. The IceCube Neutrino Observatory has already celebrated several successes such as the detection of two extragalactic neutrinos in the PeV energy range. Due to these successes several upgrades are planned, namely the IceCube Upgrade and IceCube-Gen2. The IceCube Upgrade serves to extend the energy threshold of IceCube down to the GeV level. A subsequent upgrade, IceCube-Gen2, is expected to extend the detector volume by a factor of about eight which will improve the detector efficiency in the high energy sector [2–4].

For these extensions, new optical modules have been developed to improve the precision of the detector. The main component of these modules are the photomultiplier tubes and therefore these need to be characterized and understood. The aim of this thesis is to build and commission an ellipsometer which will later be used to analyze the photocathode of photomultiplier tubes to determine a relationship between the thickness of the photocathode and the quantum efficiency. With an ellipsometer the complex refractive index N and the thickness d of layers can be determined. Here, the ellipsometer will be analyzed by measuring three different samples for two different methods of ellipsometry, namely the null ellipsometry and the rotating analyzer ellipsometry.

In the following chapter 2, the property of neutrinos, the IceCube Neutrino Observatory and the photomultiplier tubes are discussed in more detail. Afterwards, the theoretical basics, which are necessary for the understanding the function of an ellipsometer, follow in chapter 3. In addition, two different methods of ellipsometry are explained more extensively. After that, the experimental setup of the ellipsometer is shown and the characterization of the single optical components is given (cf. chapter 4). Then in chapter 5 the samples used for the analysis of the ellipsometer are explained and the measurement results of the ellipsometer are shown and compared with the expected values. Finally a short summary of the most important results and an outlook on possible improvements and applications of the setup are given in chapter 6.

2 Neutrino astronomy

This chapter gives a general overview of the properties of neutrinos and their detection, as well as a brief introduction to the IceCube Neutrino Observatory.

2.1 Neutrino properties

Neutrinos are elementary particles and belong to the leptons in the Standard Model of particle physics. They can be divided into three flavors, which are related to the charged leptons, namely electron, muon and tau neutrinos. In the Standard Model, neutrinos are considered to be massless. It was observed that the flavor of the neutrinos is not conserved during propagation. From this follows that neutrinos can change their flavor via an oscillation. Therefore, neutrinos are produced and interact as flavor eigenstates but propagate as mass eigenstates. In order for neutrinos to oscillate they have to possess mass, contrary to the assumption in the Standard Model [5]. However, their mass is very small with an upper boundary of 1.1 eV and can be considered in some cases as negligible [6].

Besides their negligible mass, neutrinos are neutrally charged particles and can only interact via the weak force. Accordingly neutrinos have a small interaction cross section and therefore interact very rarely with their environment. This results in the impossibility of a direct detection of neutrinos. Nevertheless they can be detected indirectly through secondary charged particles which are emitted after an interaction of a neutrino. This also leads to the fact that neutrinos are an important messenger for the search of cosmic ray sources in astroparticle physics because they are not deflected by galactic magnetic field during their path to the Earth [5, 7].

2.1.1 Neutrino interactions

For neutrinos with energies greater than 10 GeV the interaction with nucleons (N) is dominated by the deep inelastic scattering. Since neutrinos can only interact via the weak force, the interaction can take place through two different interaction channels which depend on the gauge bosons of the weak force. The interaction through the W-Bosons (W^\pm) is called charged current (CC) and the one via the Z-Boson (Z^0) neutral current (NC). These two interactions can be represented by

$$\bar{\nu}_\ell + N \xrightarrow{W^\pm} \ell^\mp + X \text{ (CC)}, \quad \bar{\nu}_\ell + N \xrightarrow{Z^0} \bar{\nu}_\ell + X \text{ (NC)}, \quad (2.1.1)$$

where $\bar{\nu}_\ell$ represents a (anti-)neutrino, ℓ the corresponding lepton flavor and X describes the created hadronic particles which can be one or more. The produced charged particles can be observed in a detector utilizing Cherenkov radiation [7].

2.1.2 Cherenkov radiation

If a charged particle with velocity v passes through a dielectric medium with refractive index n , the medium is polarized by inducing temporary dipoles along the particle's path. In this context, it should be mentioned that the described polarization is not an excitation or ionization of the atoms in the medium.

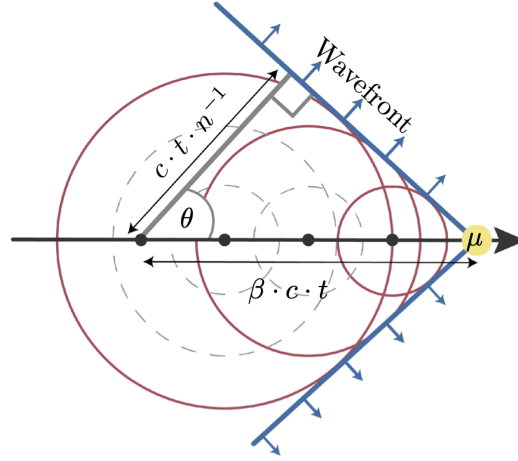


Figure 2.1.1: Illustration of a Cherenkov cone emitted by a muon. Figure taken from [8].

In case the velocity of charged particle is smaller than the speed of light in the medium $c_n = \frac{c}{n}$, the electromagnetic field interferes destructively and cannot be detected. But if the velocity is greater, the field interferes constructively and thereby photons are radiated. This radiation is known as Cherenkov radiation.

The Cherenkov radiation is emitted in a cone shape along the path of the charged particle under the Cherenkov angle Θ_C (cf. figure 2.1.1). This particular angle is defined by the Cherenkov relation

$$\Theta_C = \arccos\left(\frac{c}{n \cdot v}\right), \quad (2.1.2)$$

where c is the speed of light in vacuum [9].

The mentioned radiation is used for the indirect detection of neutrinos. For this purpose detectors with a large detection volume and a transparent detection medium, such as water or ice, are built. A large detection volume is required because of the small interaction cross-section of neutrinos. The detection medium has to be transparent such that the Cherenkov radiation produced by the charged particles is not absorbed. One possibility to detect the Cherenkov radiation is with the help of optical modules consisting of one or more photomultiplier tubes (PMTs) [1].

2.2 IceCube Neutrino Observatory

The IceCube Neutrino Observatory is a Water-Cherenkov detector located at the South Pole. Its instrumented volume includes approximately one cubic kilometer deep glacial ice. IceCube consists of a total of 5160 digital optical modules (DOMs), each equipped with one 10" photomultiplier tube (PMT) and placed on 86 strings at depths between 1450 m and 2450 m. The horizontal distance between the strings is 125 m (cf. figure 2.2.1). With IceCube, neutrinos in an energy range of about 100 GeV to several PeV can be detected. From the amount of detected photons their direction, energy, arrival time and flavor can be determined. In order to detect neutrinos with lower energies (10 GeV - 100 GeV) eight additional strings were placed in the middle of the detector, referred as DeepCore. The digital optical modules are located in a depth deeper than 1750 m and the horizontal string distance is 72 m. In addition, the strings of the DeepCore are more densely instrumented with a vertical module distance of 7 m as opposed to 10 m for the strings outside the DeepCore [2].

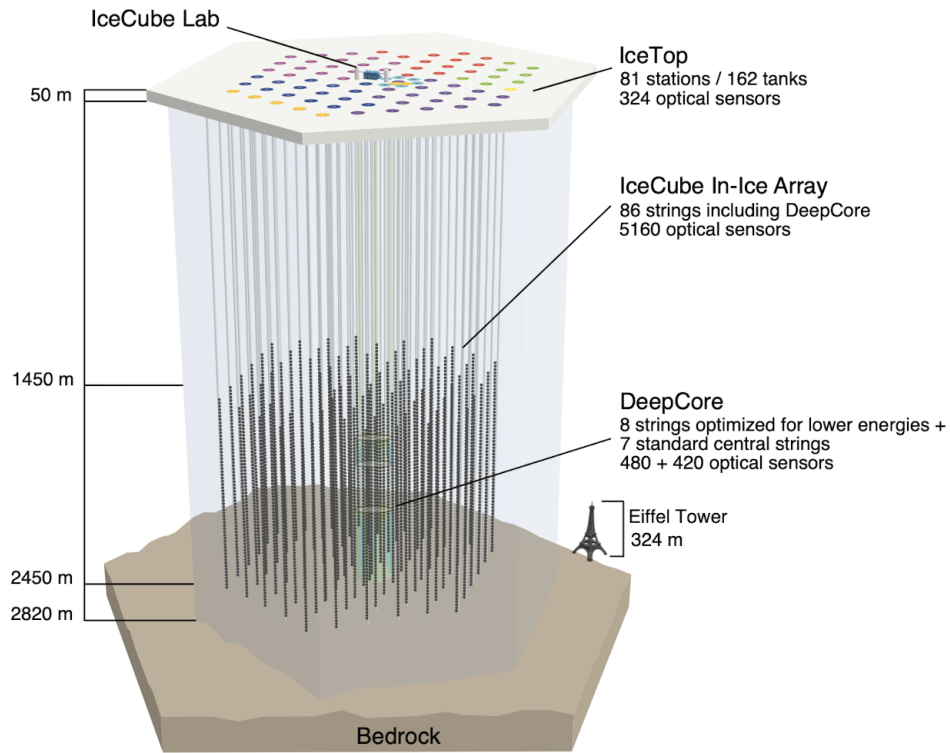


Figure 2.2.1: Schematic of the IceCube neutrino telescope. The different installation phases of the strings are represented by the colored markings. Figure taken from [2].

At the surface of the detector, 162 ice-filled tanks which are instrumented with DOMs, installed in total of 81 stations, build up a cosmic air shower array called IceTop. In addition to its usage as an air shower detector, it can also serve as a veto for atmospheric muons [2].

2.2.1 IceCube Upgrade and IceCube-Gen2

In order to improve the efficiency of the detector and increase the energy range of the detectable neutrinos, two extensions are planned for IceCube, namely IceCube Upgrade and IceCube-Gen2. Both extensions are illustrated in figure 2.2.2.

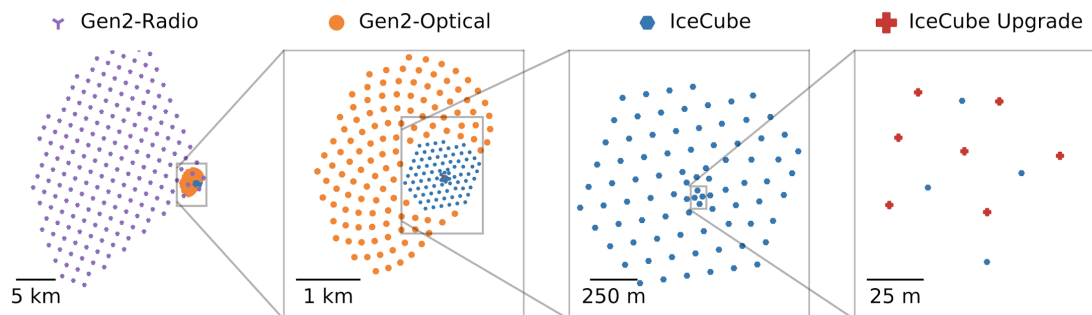


Figure 2.2.2: Illustration of the planned extensions of the IceCube neutrino telescope. Figure taken from [4].

Expected in 2023, as part of IceCube Upgrade, seven additional strings will be installed in the DeepCore, which will include a total of 693 optical sensors and will be installed in a depth of 2150 m to 2425 m. The optical sensors will contain two new optical modules, firstly the multi-PMT optical

module called mDOM and secondly the Dual optical sensor called D-Egg. The goal of this expansion is to lower the energy threshold to about 1 GeV, to open the possibility for a better calibration of the IceCube detector, to enable the tau neutrino detection and to increase the sensitivity to neutrino oscillations [3, 4].

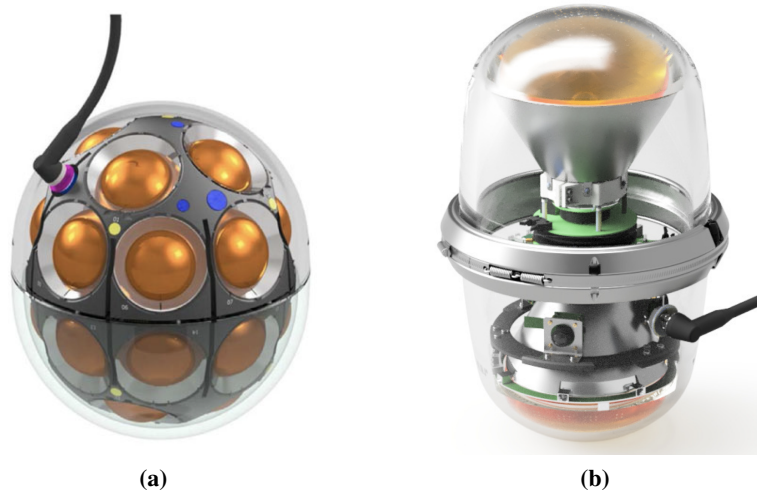


Figure 2.2.3: (a) Representation of the mDOM and (b) of the D-Egg. Figures taken from [10] and [11].

As shown in figure 2.2.3, multi-PMT modules were developed for the IceCube Upgrade. The mDOM consists of 24 3" PMTs and thus has a better angular and directional resolution and a larger photocathode area than the DOM. The D-Egg is equipped with two 8" PMTs oriented up and down. The directional resolution is therefore limited but narrower modules are possible which simplify insertion into the ice and require less power consumption [4].

The second planned upgrade of the IceCube detector, IceCube-Gen2, will extend the detector by three new parts, namely an in-ice optical array, a surface air shower array and an extended radio detector array. The in-ice optical array is intended to install 120 new strings with 80 optical modules with a horizontal distance of 240 m between them. This will increase the detection volume by a factor 7.9. The goal of the new in-ice optical array is to increase the energy range to EeV and to improve the neutrino collection rate due to the expanded volume of the detector [4].

2.2.2 Photomultiplier tubes

The optical modules which are currently and will be used in the future for IceCube and its extensions consists of one or more photomultiplier tubes (PMTs). A PMT detects light by converting the incident photons into an electrical signal. For this, the incident photons are absorbed by the photocathode and can emit photoelectrons through the photoelectric effect (cf. figure 2.2.4). If a photoelectron, also called primary electron, is released, it is guided by the focusing electrode and accelerated to the first dynode. The primary electron is multiplied at this dynode and thereby secondary electrons are produced. These electrons are further multiplied in the dynode system and finally registered at the anode [12].

The photocathode of the PMT can be investigated by using an ellipsometer. Two types of photocathodes are distinguished, the semitransparent cathodes and the opaque cathodes. The semitransparent ones are located on the inner side of the window (as shown in figure 2.2.4), while the opaque cathodes are located on a metal electrode which is mounted in the inner side of the PMT [12, 13].

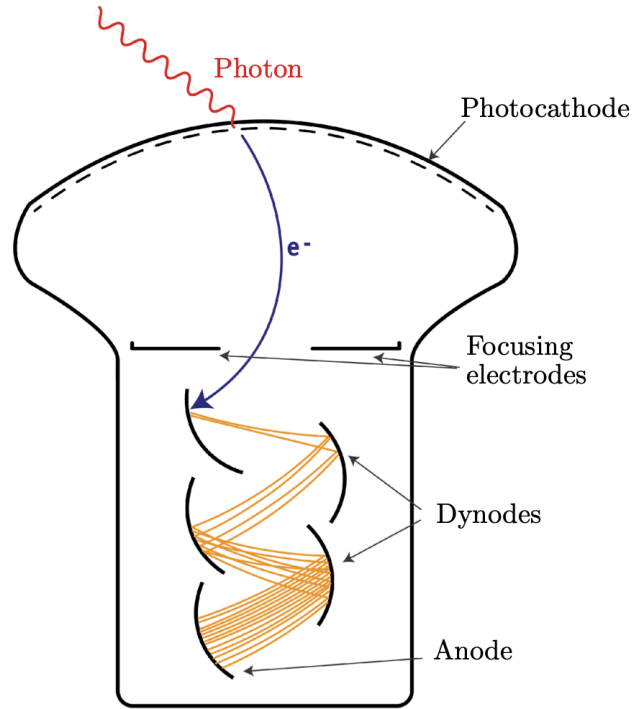


Figure 2.2.4: Illustration of the structure of a photomultiplier tube and its operation. Figure taken from [8].

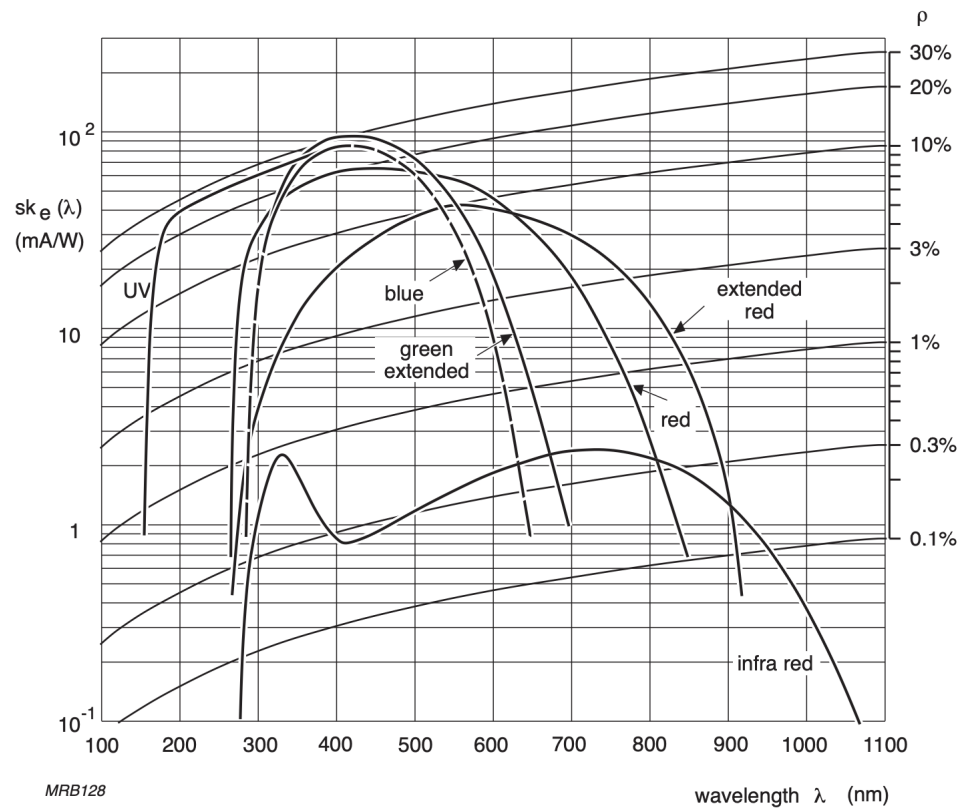


Figure 2.2.5: Spectral sensitivity characteristic for the most common photocathode materials plotted against the wavelength. Also the uniform quantum efficiency curves are shown. Figure taken from [13].

Both types of photocathode consist of photoemissive semiconductors. The most common materials for photocathodes are AgOCs, SbCs and bi- and trialkali compositions like SbKCs, SbRbCs, SbNa₂KCs. Each of these materials have a different sensitivity for different wavelengths which are shown in figure 2.2.5. This spectral sensitivity characteristic shows not only the sensitivity of different photocathode materials but also the uniform quantum efficiency ρ which describes the ratio between the number of emitted photoelectrons by the photocathode N_e and the number of incident photons N_γ and is related by

$$\rho = \frac{N_e}{N_\gamma} = S_{k,\lambda} \frac{hc_0}{\lambda e} \quad (2.2.1)$$

to the sensitivity of the photocathode $S_{k,\lambda}$. Here c_0 is the speed of light in vacuum, e is the electron charge, h the Planck's constant and λ is the wavelength [12, 13]. However, the quantum efficiency also depends on the absorption of photons and the diffusion and emission of the electron created by the photoelectric effect. For an electron to be emitted from the photocathode requires sufficient energy. Nevertheless, the electron loses different amounts of energy before diffusing through the photocathode, depending on the path length. If the path length is too long, the electron has not enough energy to escape the photocathode. Therefore, it is important to establish the relationship between quantum efficiency and photocathode thickness since the thickness has an influence on the emission of the electron and thus also on the quantum efficiency. The ellipsometer will be used to determine the influence of the thickness of the photocathode on the quantum efficiency [14].

3 Ellipsometry

In the following sections the most important theoretical basics of an ellipsometer are explained, as well as the basic design and two special types of ellipsometry.

3.1 Polarization of light

Light can be described as an electromagnetic wave. The electric field \vec{E} and the magnetic induction \vec{B} of the electromagnetic wave are perpendicular to each other, as well as to the propagation direction. The important parameter for the description of the light wave is the electric field as it describes the polarization of the light wave. If the electric field has a certain orientation, the light wave is called polarized.

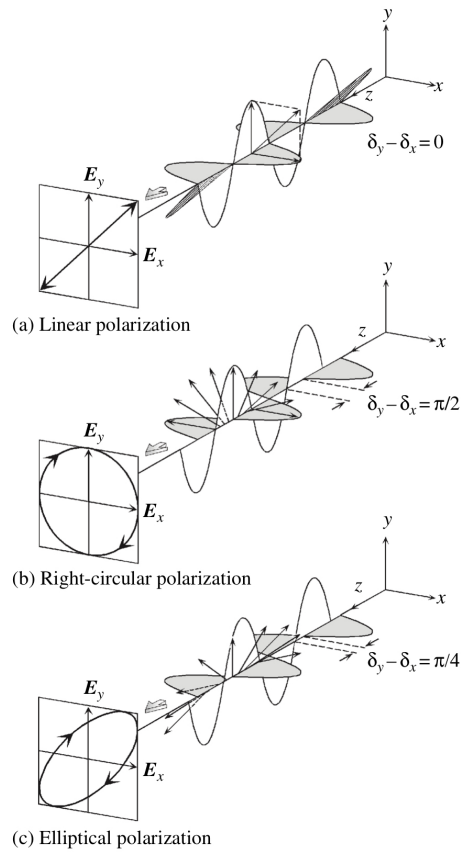


Figure 3.1.1: Illustration of different light polarizations and their relative phase differences $\delta = \delta_y - \delta_x$. In these cases the complex amplitudes of the partial waves are equal ($E_{x,0} = E_{y,0}$). Figure taken from [15].

A monochromatic plane wave, which propagates along the z-axis in a right-handed coordinate system, can be described by

$$\vec{E}(z, t) = \vec{E}_x(z, t) + \vec{E}_y(z, t) \quad (3.1.1)$$

$$= [E_{x,0} \cdot \exp(i(\omega t - Kz + \delta_x))] \cdot \vec{x} + [E_{y,0} \cdot \exp(i(\omega t - Kz + \delta_y))] \cdot \vec{y}, \quad (3.1.2)$$

where $E_{x,0}$ and $E_{y,0}$ are the complex amplitudes, ω the angular frequency and K the propagation number¹. It is evident that the wave can be described by the superposition of two partial waves, one in x-direction and one in y-direction. The phase of both partial waves is described by δ_x and δ_y . For the description of the polarization of the light wave, the relative phase difference $\delta = (\delta_y - \delta_x)$ and the relative amplitude ratio of both waves are needed. To determine the polarization, the intensity $I = E(z, t) \cdot E^*(z, t)$ of the light is measured and normalized to $I = 1$. Because of this, only the real part of the electric field is relevant [15, 16].

The polarization of the light can be divided into linear, circular and elliptical polarized. A light wave has a linear polarization, if the relative phase difference is a multiple of π ($\delta = 0, \pm\pi, \dots$). In this case, the electric field vector is aligned in one specific direction. If $E_{x,0} = E_{y,0}$, the electric field vector is aligned at 45° as shown in figure 3.1.1 (a). If the relative phase difference is a multiple of $\frac{\pi}{2}$ ($\delta = \pm\frac{\pi}{2}, \pm\frac{3\pi}{2}$) and also assumes that $E_{x,0} = E_{y,0}$, the light is called circular polarized. This results in the electric field vector starting to rotate and thereby it can be distinguished between two types of circular polarization. If the relative phase difference is positive, the light is right-circular polarized (cf. figure 3.1.1 (b)). This means that the electric field vector rotates clockwise. If, on the other hand, the relative phase difference is negative, the polarization is called left circular. Then, the electric field vector rotates counterclockwise. In all other cases, the light is elliptically polarized. In figure 3.1.1 (c) it is shown for the case $\delta = \frac{\pi}{4}$ and $E_{x,0} = E_{y,0}$ [15].

3.2 Jones vectors and Jones matrices

To be able to analyze optical measurements, a mathematical explanation is necessary. Such is given by the Jones vectors and Jones matrices which are the topics of the next sections 3.2.1 and 3.2.2.

3.2.1 Jones vectors

The Jones vector describes the polarization of light. It can be defined as a column vector

$$\vec{E}(z, t) = \begin{bmatrix} E_x \\ E_y \end{bmatrix} = \begin{bmatrix} E_{x,0} \exp(i\delta_x) \\ E_{y,0} \exp(i\delta_y) \end{bmatrix}, \quad (3.2.1)$$

which shows the electric field of the partial waves in x- and y- direction. It is assumed that the light wave propagates in z-direction for a right handed coordinate system as discussed in section 3.1. The equation can also be represented as follows

$$E_x = |E_x| \exp(i\Delta) \quad (3.2.2)$$

$$E_y = |E_y|, \quad (3.2.3)$$

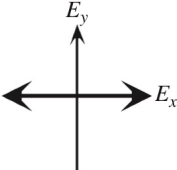
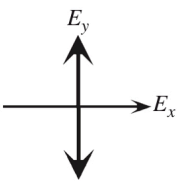
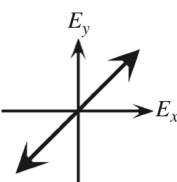
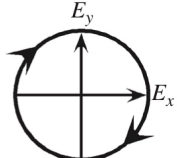
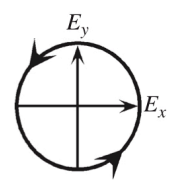
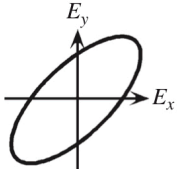
where $\Delta = \delta_x - \delta_y$ is the phase difference between the partial waves. Elliptic polarized light can be expressed by

$$E_{elli} = \begin{bmatrix} \sin(\Psi) \exp(i\Delta) \\ \cos(\Psi) \end{bmatrix} \quad (3.2.4)$$

¹Here the propagation number is defined by K instead of k , because the complex refractive index is denoted by k .

with $\tan(\Psi) = \frac{E_{x,0}}{E_{y,0}}$ which stands for the relative amplitude ratio. The parameter Δ and Ψ are also called the ellipsometric angles which are necessary for the determination of polarized light and will be measured in the ellipsometry. The Jones vectors for linear polarized and circular polarized light are shown in table 3.2.1 [15, 16].

Table 3.2.1: Representation of the Jones and Stokes vectors (cf. section 3.3) for different light polarizations. Table taken from [15].

| Polarization | Polarization state | Jones vector | Stokes vector |
|--|---|--|---|
| Linear polarization parallel to x axis |  | $\begin{bmatrix} 1 \\ 0 \end{bmatrix}$ | $\begin{bmatrix} 1 \\ 1 \\ 0 \\ 0 \end{bmatrix}$ |
| Linear polarization parallel to y axis |  | $\begin{bmatrix} 0 \\ 1 \end{bmatrix}$ | $\begin{bmatrix} 1 \\ -1 \\ 0 \\ 0 \end{bmatrix}$ |
| Linear polarization oriented at 45° |  | $\frac{1}{\sqrt{2}} \begin{bmatrix} 1 \\ 1 \end{bmatrix}$ | $\begin{bmatrix} 1 \\ 0 \\ 1 \\ 0 \end{bmatrix}$ |
| Right-circular polarization |  | $\frac{1}{\sqrt{2}} \begin{bmatrix} 1 \\ i \end{bmatrix}$ | $\begin{bmatrix} 1 \\ 0 \\ 0 \\ 1 \end{bmatrix}$ |
| Left-circular polarization |  | $\frac{1}{\sqrt{2}} \begin{bmatrix} 1 \\ -i \end{bmatrix}$ | $\begin{bmatrix} 1 \\ 0 \\ 0 \\ -1 \end{bmatrix}$ |
| Elliptical polarization |  | $\begin{bmatrix} \sin \psi \exp(i\Delta) \\ \cos \psi \end{bmatrix}$ | $\begin{bmatrix} 1 \\ -\cos 2\psi \\ \sin 2\psi \cos \Delta \\ -\sin 2\psi \sin \Delta \end{bmatrix}$ |
| Natural light (unpolarized light) | | | $\begin{bmatrix} 1 \\ 0 \\ 0 \\ 0 \end{bmatrix}$ |

3.2.2 Jones matrices

The optical elements which are used in the measurements can be described by the Jones matrices. Important components of ellipsometry are polarizers (analyzers) and compensators. A polarizer (analyzer) can be used to convert unpolarized light into linear polarized light. The Jones matrix for a linear polarizer \mathbf{P} (linear analyzer \mathbf{A}) is defined as follows

$$\mathbf{P} = \mathbf{A} = \begin{bmatrix} 1 & 0 \\ 0 & 0 \end{bmatrix}. \quad (3.2.5)$$

In this case the polarizer angle is parallel to the x-axis.

A quarter-wave plate has a fast and a small axis. Using this optical element can cause a phase difference between the electric field vectors because the light which is parallel to the fast axis propagate faster through the quarter-wave plate than the light parallel to the slow axis. If a compensator \mathbf{C} is considered which has its fast axis parallel to the x-axis, the following Jones matrix can be applied

$$\mathbf{C} = \begin{bmatrix} 1 & 0 \\ 0 & \exp(i\delta) \end{bmatrix}, \quad (3.2.6)$$

where δ is the phase shift caused by the compensator. The sample \mathbf{S} can also be described by a Jones matrix

$$\mathbf{S} = \begin{bmatrix} \sin(\psi) \exp(i\Delta) & 0 \\ 0 & \cos(\psi) \end{bmatrix} \quad (3.2.7)$$

which contains the two ellipsometry parameter ψ and Δ . To calculate the change of the polarization of the light which is caused by the optical elements, the Jones matrices are multiplied with the Jones vector of the incident light [15, 16]. Thus the effect of a polarizer is described as

$$\vec{E}_{\text{out}} = \mathbf{P} \cdot \vec{E}_{\text{in}}. \quad (3.2.8)$$

If several optical elements are used and their axes are not parallel to the x-axis, a rotation of the coordinate system is needed since the Jones matrices refer to the original coordinate system. This rotation can be described by a rotation matrix \mathbf{R} which is defined as follows

$$\mathbf{R}(\alpha) = \begin{bmatrix} \cos(\alpha) & \sin(\alpha) \\ -\sin(\alpha) & \cos(\alpha) \end{bmatrix}. \quad (3.2.9)$$

For a positive α , the rotation is specified as clockwise [15]. As an example, when light is going through a polarizer at an angle α and then through an analyzer parallel to the x-axis, then the light measured by a light detector can be determined by

$$\vec{E}_{\text{out}} = \mathbf{A} \cdot \mathbf{R}(-\alpha) \cdot \mathbf{P} \cdot \vec{E}_{\text{in}}. \quad (3.2.10)$$

3.3 Stokes formalism

Another possibility besides the Jones vectors to identify the polarization of light is given by the Stokes formalism. Besides totally polarized light, partially polarized and unpolarized light can also

be described. The Stokes vector consists of four parameters that are defined as follows:

$$S_0 = I_x + I_y, \quad (3.3.1)$$

$$S_1 = I_x - I_y, \quad (3.3.2)$$

$$S_2 = I_{45^\circ} - I_{-45^\circ}, \quad (3.3.3)$$

$$S_3 = I_R - I_L, \quad (3.3.4)$$

where S_0 represents the total light intensity and S_{1-3} the relative intensity difference between different states of polarization. S_1 describes the relative intensity difference between linear polarized light in x- (I_x) and y-direction (I_y). Also, S_2 shows the difference between linear polarized light, however, for the angular alignments 45° (I_{45°) and -45° (I_{-45°). The relative intensity difference between right circular polarized (I_R) and left circular polarized light (I_L) is specified by S_3 . Thus, four parameters can be represented as a sphere, such as the one shown in figure 3.3.1. This is called Poincaré sphere. The parameters S_{1-3} serve as axes of the coordinate system and S_0 defines the radius of the sphere. The sphere can be used to characterize the polarization of light. If the sphere is considered as a globe, then the light is linearly polarized at the equator and circularly polarized at the poles. Between the equator and the poles the light is elliptically polarized [15].

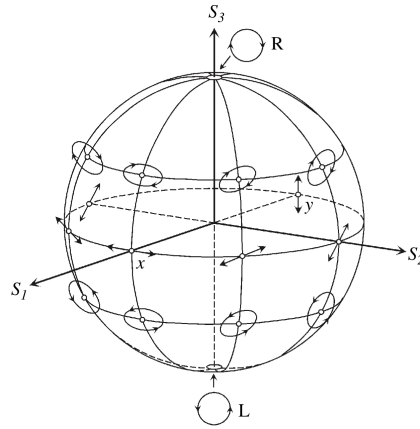


Figure 3.3.1: Representation of the polarization of light in a Poincaré sphere. At the equator the light is linear polarized and at the poles it is circular polarized. In between, the light is elliptically polarized. Figure taken from [15].

If light is totally polarized, the length of the vector to the point $P = (S_1, S_2, S_3)^T$ on the sphere describes the total light intensity S_0 (cf. figure 3.3.2 (a)) and can be calculated with the following equation:

$$S_0^2 = S_1^2 + S_2^2 + S_3^2. \quad (3.3.5)$$

The equation is changed to

$$S_0^2 > S_1^2 + S_2^2 + S_3^2, \quad (3.3.6)$$

if the light is partially polarized. Partially polarized light results in a distribution of points on the sphere around the point P (cf. figure 3.3.2 (b)) because the polarization changes with time. For unpolarized light the points on the sphere are distributed around the complete sphere, as shown in figure 3.3.2 (c), because there is no specific polarization. With the Stokes parameters a degree of

polarization p can be calculated by

$$p = \frac{\sqrt{S_1^2 + S_2^2 + S_3^2}}{S_0}. \quad (3.3.7)$$

For $p = 0$ the light is unpolarized and for $p = 1$ it is totally polarized, whereas the light is partially polarized for $0 < p < 1$ [15].

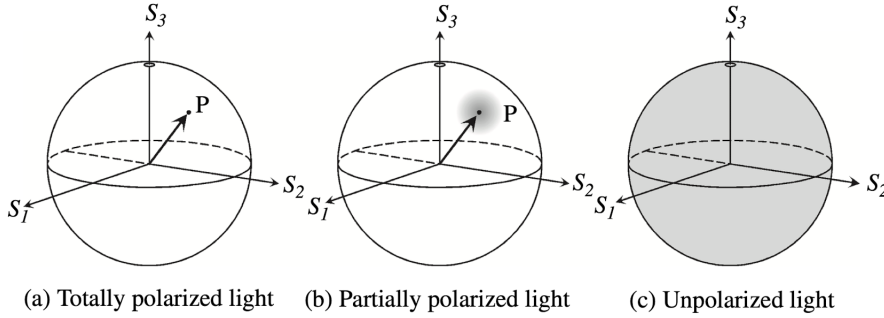


Figure 3.3.2: Pointcaré sphere for (a) totally polarized, (b) partially polarized and (c) unpolarized light. Figure taken from [15].

In the Stokes formalism, like in the Jones formalism (cf. section 3.2.2), the optical elements are represented by matrices. The Mueller matrix for a linear polarizer \mathbf{P} (analyzer \mathbf{A}) at an angle α is defined as follows:

$$\mathbf{P} = \mathbf{A} = \frac{1}{2} \begin{bmatrix} 1 & \cos(2\alpha) & \sin(2\alpha) & 0 \\ \cos(2\alpha) & \cos^2(2\alpha) & \sin(2\alpha)\cos(2\alpha) & 0 \\ \sin(2\alpha) & \sin(2\alpha)\cos(2\alpha) & \sin^2(2\alpha) & 0 \\ 0 & 0 & 0 & 0 \end{bmatrix} \quad (3.3.8)$$

and for a compensator \mathbf{C} at angle α

$$\mathbf{C} = \begin{bmatrix} 1 & 0 & 0 & 0 \\ 0 & \cos(2\alpha)^2 + \cos(\delta)\sin(2\alpha)^2 & \sin(2\alpha)\cos(2\alpha)(\cos(\delta) - 1) & \sin(\delta)\sin(2\alpha) \\ 0 & \sin(2\alpha)\cos(2\alpha)(\cos(\delta) - 1) & \sin(2\alpha)^2 + \cos(\delta)\cos(2\alpha)^2 & \sin(\delta)\cos(2\alpha) \\ 0 & -\sin(\delta)\sin(2\alpha) & -\sin(\delta)\cos(2\alpha) & \cos(\delta) \end{bmatrix}, \quad (3.3.9)$$

where δ is the phase shift caused by the compensator [16].

3.4 Reflection and Transmission

3.4.1 Reflection at an interface

If light, which is assumed to be a monochromatic plane wave, strikes the interface between two semi-infinite media in an oblique incidence, a reflected and a transmitted partial wave are produced [16]. Figure 3.4.1 shows this schematically in a right-handed coordinate system.

The angle of incidence φ_1 of the plane wave is equal to the angle of the reflected wave. To determine the angle of the transmitted wave φ_2 Snell's law

$$N_1 \sin(\varphi_1) = N_2 \sin(\varphi_2) \quad (3.4.1)$$

is applied. Snell's Law gives the relationship between the transmission and incidence angles, as well as the relationship between the refractive indices N_1, N_2 of the two media. The refractive indices are complex and have the following form

$$N_j = n_j + ik_j, \quad (3.4.2)$$

where n_j is the refractive index and k_j is the extinction coefficient of the medium [15].

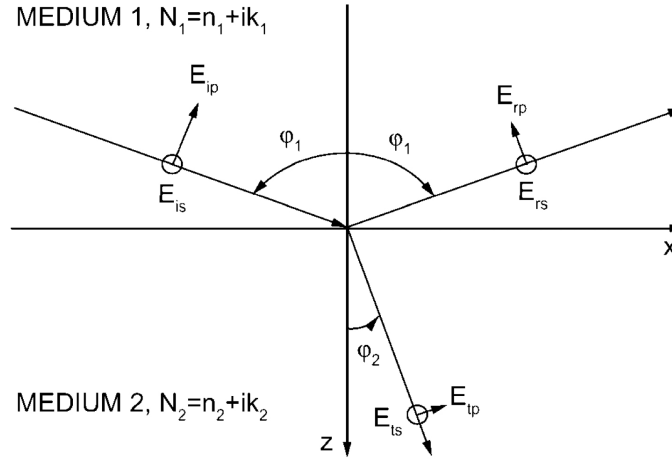


Figure 3.4.1: Illustration of the reflected and transmitted partial waves, if a monochromatic plane wave strikes the interface between two infinite media at an oblique incidence. N_1 and N_2 are the complex refractive index of the two media. The indices p and s describe, if it is p- or s-polarized light and the indices i, r, t stand for the incidence, reflected and transmitted light. Figure taken from [16].

The light wave can be divided into p- and s-polarized light. Whether the light is p- or s-polarized is determined by the oscillation direction of the electric field. The oscillation direction of the electric field of the p-polarized light is in the x-z plane, the so called plane of incidence. The oscillation of the s-polarized light is perpendicular to the plane of incidence [15].

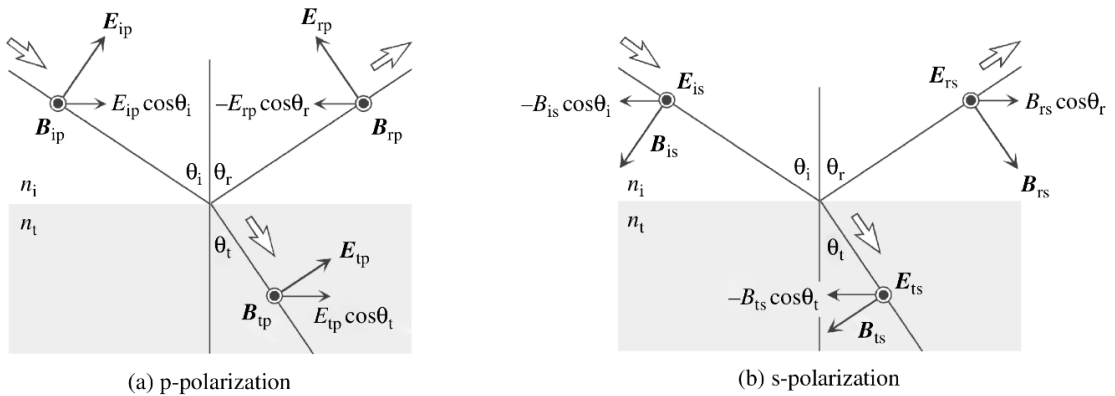


Figure 3.4.2: Schematic description of the expression of light by the electric field \vec{E} and the magnetic induction \vec{B} for p- and s-polarized light. The indices i, r, t stand for the incidence, reflected and transmitted light. Figure taken from [15].

The reflected and transmitted light can also be expressed by the electric field \vec{E} and magnetic induction \vec{B} as shown in figure 3.4.2. This results in the following boundary conditions

$$E_{ip} \cos(\theta_i) - E_{rp} \cos(\theta_r) = E_{tp} \cos(\theta_t), \quad (3.4.3)$$

$$B_{ip} + B_{rp} = B_{tp}, \quad (3.4.4)$$

for the p-polarized and

$$B_{rs} \cos(\theta_r) - B_{is} \cos(\theta_i) = -B_{ts} \cos(\theta_t), \quad (3.4.5)$$

$$E_{is} + E_{rs} = E_{ts}, \quad (3.4.6)$$

for the s-polarized light. The indices i, r, t stand for the incidence, reflected and transmitted light, respectively. In a medium, it can be assumed that $E = \frac{c}{n} \cdot B$, where n is the refractive index and c the speed of light in vacuum. If the equations 3.4.4 and 3.4.5 are rewritten by this assumption and inserted into the respective boundary condition, the amplitude reflection r and transmission coefficient t can be determined. The coefficients are defined as follows:

$$r_s = \frac{E_{rs}}{E_{is}} = \frac{n_i \cos \theta_i - n_t \cos \theta_t}{n_i \cos \theta_i + n_t \cos \theta_t}, \quad r_p = \frac{E_{rp}}{E_{ip}} = \frac{n_t \cos \theta_i - n_i \cos \theta_t}{n_t \cos \theta_i + n_i \cos \theta_t}, \quad (3.4.7)$$

$$t_s = \frac{E_{ts}}{E_{is}} = \frac{2n_i \cos \theta_i}{n_i \cos \theta_i + n_t \cos \theta_t}, \quad t_p = \frac{E_{tp}}{E_{ip}} = \frac{2n_i \cos \theta_i}{n_t \cos \theta_i + n_i \cos \theta_t}. \quad (3.4.8)$$

These coefficients are known as Fresnel coefficients and are valid for the complex refractive index. If the coefficients are represented in polar coordinates

$$r_p = |r_p| \exp(i\delta_{rp}), \quad r_s = |r_s| \exp(i\delta_{rs}), \quad (3.4.9)$$

$$t_p = |t_p| \exp(i\delta_{tp}), \quad t_s = |t_s| \exp(i\delta_{ts}), \quad (3.4.10)$$

the light reflection and transmission is due to a change in phase and amplitude [15].

Figure 3.4.3 shows the behavior of the phases and amplitudes for an air/glass interface for different angles of incidence. At the angle θ_B the p-polarized light does not reflect $|r_p| = 0$ and is called the Brewster angle. Therefore, at this angle only s-polarized light is reflected [15].

Since s- and p-polarized light undergo different changes in phase and amplitude when reflected, the amplitude ratio ψ and the phase change Δ between s- and p-polarized light is used to express the variation in polarization state. The two parameters are defined by the ratio of the reflection coefficients:

$$\rho \equiv \frac{r_p}{r_s} \equiv \tan(\psi) \exp(-i\Delta) \equiv \frac{E_{rp}E_{is}}{E_{rs}E_{ip}}. \quad (3.4.11)$$

For the description of the reflection coefficients in polar coordinates, the following definitions result:

$$\tan(\psi) = \frac{|r_p|}{|r_s|}, \quad (3.4.12)$$

$$\Delta = \delta_{rp} - \delta_{rs}. \quad (3.4.13)$$

The thickness and the complex refraction index of the analyzed layer can be determined by the ellipsometry parameters ψ and Δ [15].

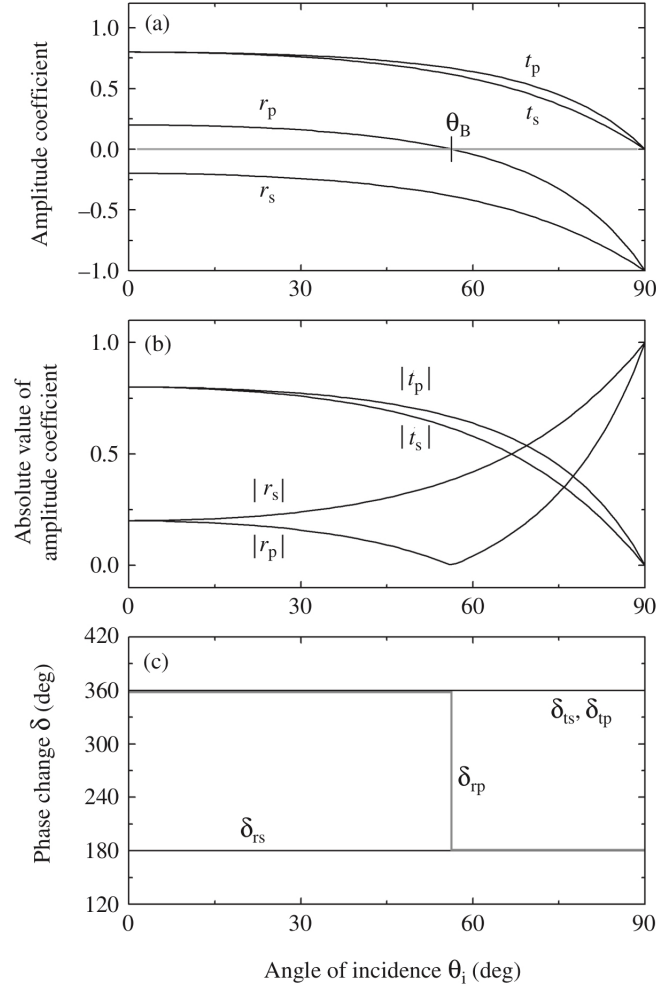


Figure 3.4.3: The amplitude coefficient (a), the absolute value of the amplitude coefficient (b) and the phase change (c) for the Fresnel coefficients at an air/glass interface are shown for different incident angles. Figure taken from [15].

3.4.2 Reflection at a three layer system

An important component of ellipsometry is the determination of layer thickness. As an example, the reflection at a three layer system, consisting of ambient, thin film with thickness d and substrate, is considered. In figure 3.4.4 such a system is shown. Each layer has a different complex refractive index. A part of the incidence light beam will be reflected at the surface (first beam) and the other part will be transmitted into the thin layer. The transmitted beam can be reflected at the interface between the thin layer and then transmitted at the surface (second beam). This beam and the first reflected beam can interfere with each other because of the phase variation

$$\beta = \frac{2\pi d}{\lambda} N_1 \cos(\theta_1), \quad (3.4.14)$$

caused by the passage of one wave through the thin layer. λ corresponds to the wavelength of the incident beam. As shown in figure 3.4.4, the beam repeats the reflection and transmission steadily, resulting in an overlapping of several beams.

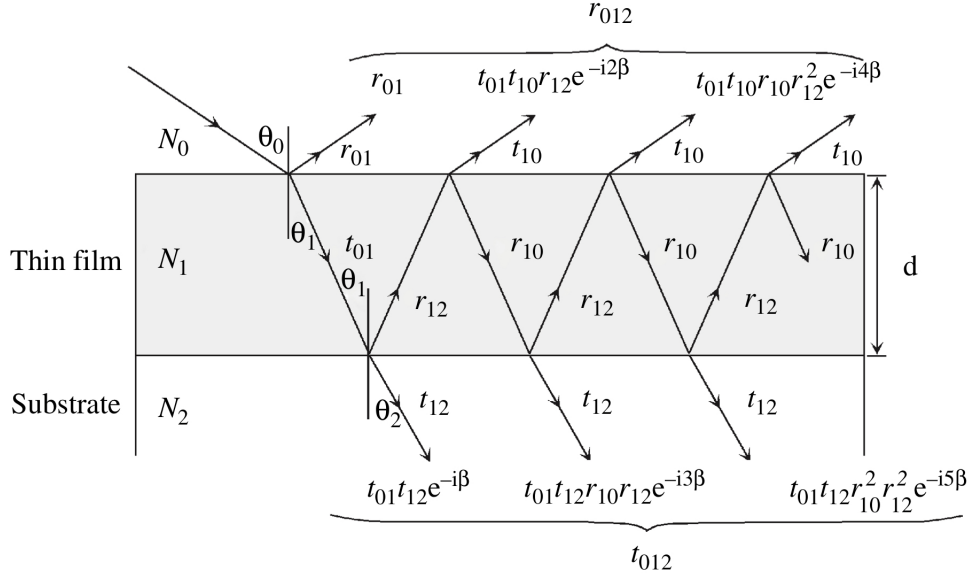


Figure 3.4.4: The reflection r_{jk} and transmission t_{jk} coefficients for a three layer system consisting of ambient, thin film and substrate are shown. d describe the thickness of the thin film. Figure taken from [15].

This overlapping can be represented by the amplitude coefficients of the layers and so the amplitude reflection coefficients r_{012} for a three layer system can be calculated. For this, each beam is described by the respective coefficients and then added to the other rays. The resulting equation has the following form:

$$r_{012} = r_{01} + t_{01}t_{10}r_{12} \exp(-i2\beta) + \dots, \quad (3.4.15)$$

where r_{01} specifies the first beam and the second summand the second beam. The equation 3.4.15 can be simplified to

$$r_{012} = r_{01} + \frac{t_{01}t_{10}r_{12} \exp(-i2\beta)}{1 - r_{01}r_{12} \exp(-i2\beta)} \quad (3.4.16)$$

using the series $y = \frac{a}{(1-r)}$. With the correlations $r_{01} = r_{10}$ and $t_{01}t_{10} = 1 - r_{01}^2$, the result is for the amplitude reflection coefficient

$$r_{012} = \frac{r_{01} + r_{12} \exp(-i2\beta)}{1 + r_{10}r_{12} \exp(-i2\beta)} \quad (3.4.17)$$

and for the amplitude transmission coefficient

$$t_{012} = \frac{t_{01}t_{12} \exp(-i2\beta)}{1 + r_{10}r_{12} \exp(-i2\beta)}. \quad (3.4.18)$$

3.5 Principle of Ellipsometry

Ellipsometry is one of the optical methods used to determine surface properties, such as the refractive index or thickness of layers or substrates. To be able to specify these properties, the change in polarization of the light after reflection on a sample is examined. This change in polarization is described by the two ellipsometry parameters ψ and Δ (cf. section 3.4.1) [15].

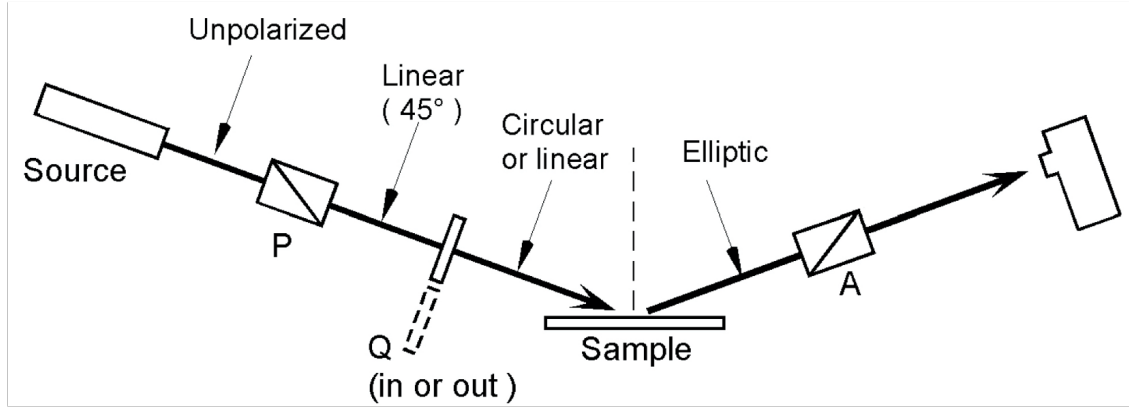


Figure 3.5.1: Illustration of the general setup of an ellipsometer. P, Q and A stand for the optical components polarizer, quarter-wave plate and analyzer. Figure taken from [16] and modified.

Figure 3.5.1 shows the general setup of an ellipsometer. The unpolarized light from a laser is sent through a polarizer (P) to get linear polarized light. Then, the light beam is passed through a quarter-wave plate (Q) to obtain circularly polarized light before it is reflected at the sample. After the reflection, the light beam goes through an analyzer (A) and the intensity of the light beam is measured with a photodiode [16].

There are many different ways to perform an ellipsometry measurement, two of the most widely used methods are presented in the following sections.

3.5.1 Null Ellipsometry

Null ellipsometry is a common configuration as it can be done without extensive technical equipment. The setup of a null ellipsometry (cf. figure 3.5.2) measurement is similar to the general setup.

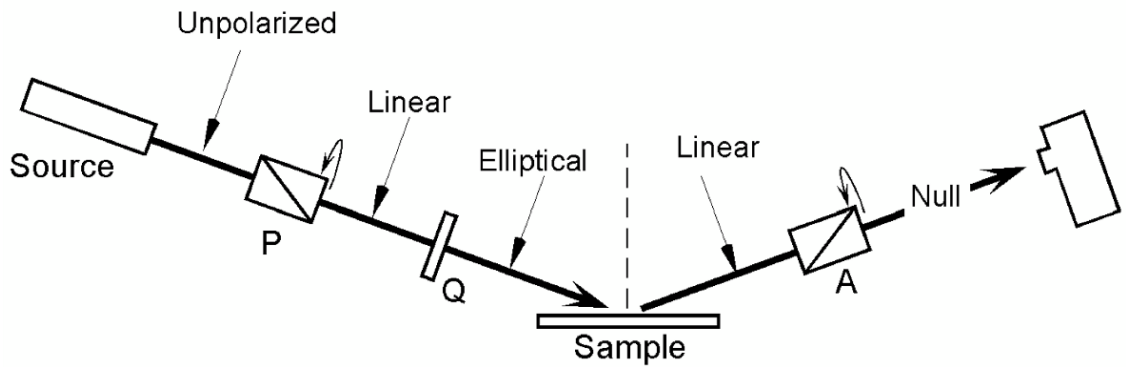


Figure 3.5.2: General setup of a null ellipsometry. The polarizer P and analyzer A are rotated and the quarter-wave plate Q remains at one angle, usually 45°. Figure taken from [16].

The goal of the null ellipsometry is to get linear polarized light after it is reflected at the sample which is extinguished by the appropriate analyzer setting. If the setup is described by the Jones formalism (cf. section 3.2)

$$\vec{E}_{out} = \mathbf{AR}(A)\mathbf{SR}(-C)\mathbf{CR}(C)\mathbf{R}(-P)\mathbf{P}\vec{E}_{in}, \quad (3.5.1)$$

the following equation results

$$E_A = r_p \cos(A) \cdot [\cos(C) \cos(P - C) - \rho_C \sin(C) \sin(P - C)] + r_s \sin(A) \cdot [\sin(C) \cos(P - C) + \rho_C \cos(C) \sin(P - C)], \quad (3.5.2)$$

where P is the polarizer angle, A the analyzer angle, C the angle of the quarter wave plate and ρ_C the phase shift of the quarter wave plate. If an intensity of zero ($E_A = 0$) and a quarter wave plate angle of $C = 45^\circ$ are assumed, the following relationship between the two ellipsometry parameters and the polarizer and analyzer angle arises

$$\psi = A \quad (A \geq 0) \quad (3.5.3)$$

$$\Delta = 2P + \frac{\pi}{2} \quad (3.5.4)$$

with the help of equation 3.4.11. In order to determine the two ellipsometry parameters, null ellipsometry only requires the angles of the polarizer and analyzer at which an intensity of zero is measured [15, 16].

3.5.2 Rotating Analyzer Ellipsometry

Another type of ellipsometry is the rotating analyzer ellipsometry. Its setup is shown in figure 3.5.3. The setup basically does not differ from the setup of the null ellipsometry (cf. figure 3.5.2), except that the polarizer angle is not changed during the measurement, only the analyzer is rotating with an angular speed of ω .

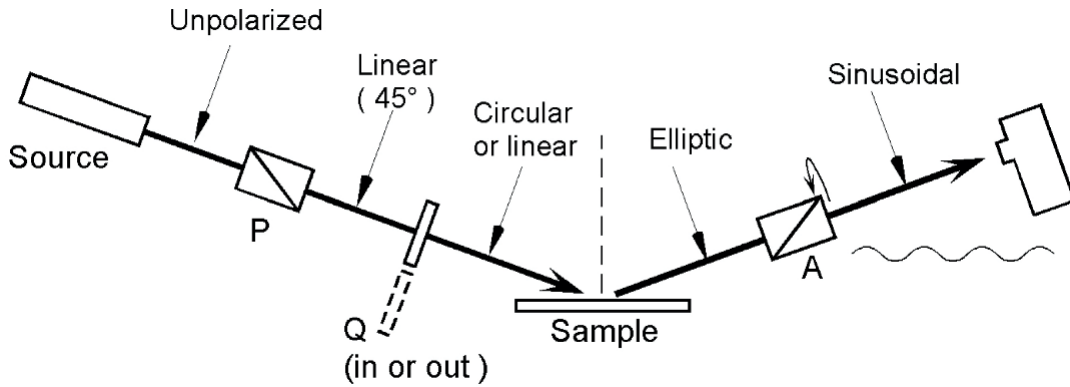


Figure 3.5.3: General setup of a rotating analyzer ellipsometry measurement. The polarizer P and the quarter-wave plate Q are at a specific angle and the analyzer A is rotated. Figure taken from [16].

This results in a correlation of $A = \omega t$ with time t for the angles. If the setup is expressed by the Jones formalism (cf. section 3.2)

$$\vec{E}_{out} = \mathbf{A}\mathbf{R}(A)\mathbf{S}\mathbf{R}(-C)\mathbf{C}\mathbf{R}(C)\mathbf{R}(-P)\mathbf{P}\vec{E}_{in}, \quad (3.5.5)$$

and it is assumed that the quarter wave plate is parallel to the x-axis, the following equation is obtained

$$E_A = \cos(A) \sin(\psi) \cos(P) \exp(i(\Delta - \delta)) + \sin(A) \cos(\psi) \sin(P). \quad (3.5.6)$$

Thus, the following equation results for the intensity

$$\begin{aligned}
 I &= |E_A|^2 \\
 &= I_0 \left[1 + \frac{\cos(2P) - \cos(2\psi)}{1 - \cos(2P) \cos(2\psi)} \cos(2A) + \frac{\sin(2P) \sin(2\psi) \cos(\Delta - \delta)}{1 - \cos(2P) \cos(2\psi)} \sin(2A) \right] \\
 &= I_0 [1 + \alpha \cos(2A) + \beta \sin(2A)],
 \end{aligned} \tag{3.5.7}$$

where α and β are the normalized Fourier coefficients. It can be seen that the intensity changes with the analyzer angle A . The two Fourier coefficients can be rewritten in

$$\alpha = \frac{\tan(\psi)^2 - \tan(P)^2}{\tan(\psi)^2 + \tan(P)^2}, \tag{3.5.8}$$

$$\beta = \frac{2 \tan \psi \cos(\Delta - \delta) \tan(P)}{\tan(\psi)^2 + \tan(P)^2} \tag{3.5.9}$$

and the following relationships to the two ellipsometry parameters

$$\tan(\psi) = \sqrt{\frac{1+\alpha}{1-\alpha}} |\tan(P)|, \quad \cos(\Delta - \delta) = \frac{\beta}{\sqrt{1-\alpha^2}} \tag{3.5.10}$$

are concluded. With the help of α and β , the Stokes parameters (cf. section 3.3) can also be determined with the equations

$$\alpha = S_1, \quad \beta = S_2 \cos(\delta) - S_3 \sin(\delta). \tag{3.5.11}$$

To obtain the values of S_2 and S_3 , two measurements with different phase shifts δ are needed [15].

3.6 Rotating Quarter-Wave Plate Stokes Polarimeter

To specify the polarization of light a polarimeter is required. There are many different types of polarimeters. One of them is the rotating quarter-wave plate stokes polarimeter which consists of a quarter-wave plate and a polarizer as shown in figure 3.6.1.

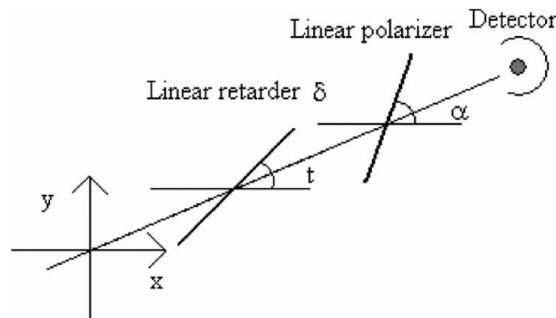


Figure 3.6.1: Illustration of the setup of a rotating quarter-wave plate stokes polarimeter. Here a left-handed coordinate system is used instead of a right-handed one. Figure taken from [17].

With this optical instrument, the Stokes parameters (cf. section 3.3) can be determined with the following equation

$$\vec{S}_{\text{out}} = \mathbf{P}(\alpha) \cdot \mathbf{C}(\delta, t) \cdot \vec{S}_{\text{in}}, \tag{3.6.1}$$

where \vec{S}_{in} and \vec{S}_{out} are the input and output Stokes vectors, $\mathbf{P}(\alpha)$ the Mueller matrix for the polarizer with an angle α and $\mathbf{C}(\delta, t)$ the Mueller matrix for the quarter wave plate at angle t and its phase shift δ . The Stokes formalism was used here instead of the Jones formalism because it can describe partial and unpolarized light.

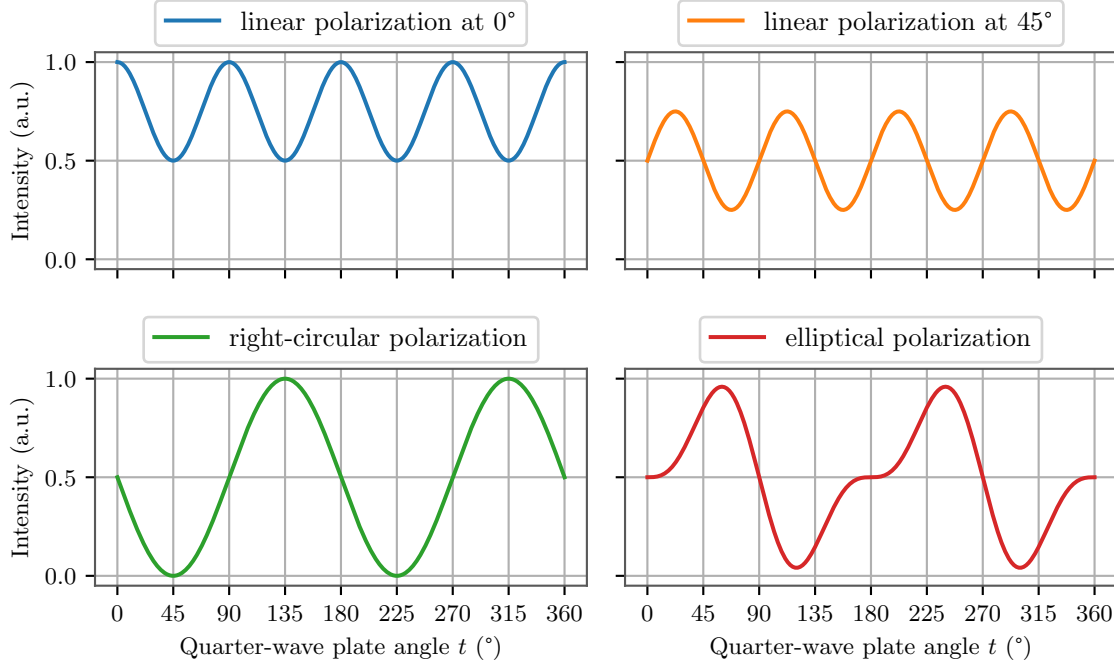


Figure 3.6.2: The theoretical expected intensity curves for different light polarizations measured with a rotating quarter-wave plate Stokes polarimeter are shown.

With this equation the intensity of the measured output beam can be calculated. If it is assumed that the polarizer is at an angle of $\alpha = 0^\circ$ and the phase shift is $\delta = \frac{\pi}{2}$, following equation

$$I(S_0, S_1, S_2, S_3, \frac{\pi}{2}, t, 0) = \frac{S_0}{2} + \frac{S_1}{2} \left(\frac{1}{2} + \frac{1}{2} \cos(4t) \right) + \frac{S_2}{4} \sin(4t) - \frac{S_3}{2} \sin(2t) \quad (3.6.2)$$

for the intensity results. It can be seen that the intensity depends only on the angle of the quarter-wave plate. However, it must be noted that a left-handed coordinate system is used here and not a right-handed one as before [17]. Figure 3.6.2 shows the theoretical expected intensity curves for different polarizations. The Stokes vectors shown in figure 3.2.1 are used as Stokes parameters. For the elliptically polarized light, the ellipsometry parameters are chosen to be $\psi = 45^\circ$ and $\Delta = 135^\circ$.

4 Setup and characterization of the ellipsometer

The following sections first describes the measurement setup and how to align and clean the components. This is followed by the characterization of the optical components, the laser and the angle of incidence.

4.1 Ellipsometry setup

Figure 4.1.1 shows the basic setup of the ellipsometer being used. The ellipsometer consists of two arms and a hexapod². The left arm of the ellipsometer is firmly attached to the ground plate of the ellipsometer. The right arm on the other hand is mounted on a rotation table³ which is located under the hexapod. This allows ellipsometry measurements at different incidence angles. The rotation table can manually be moved by 360° but is limited to 6° when motorized [18].

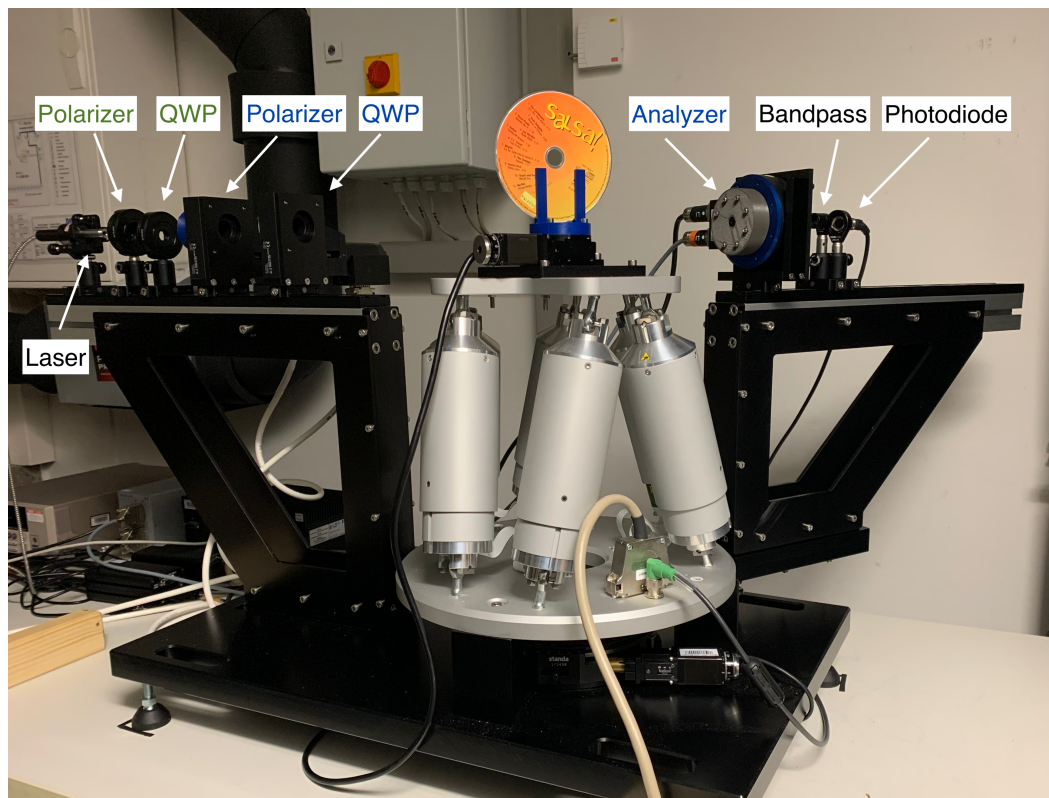


Figure 4.1.1: A picture of the general setup of the ellipsometer. The optical components labeled in blue are mounted in motorized rotation tables and the optical components described in green font are mounted in manually rotatable rotation tables.

²PI H-820 6-Axis Hexapod

³Standa 8MR170-190 - Motorized Rotary Stages

Due to the fact that the hexapod is not mounted on the rotation stage but is supported by three feet, the possible angles of incidence are limited to a range of 25° to 65° . The hexapod and the small rotation table⁴ mounted on it are used to align the sample or later the photomultiplier tube which enable the measurement of different positions on the sample. The hexapod can be moved in the x , y and z direction as well as with the angles Θ_x , Θ_y and Θ_z . The small rotation table is motorized and can be rotated 360° with an accuracy of $0.6'$ [19]. This allows an exact adjustment of the incident angle.

In order to align the components to the center of the rail, the required optical components for the ellipsometer are mounted with slides on the rails of the arms. The optical components shown in figure 3.5.1 are assembled on motorized rotation tables. The mount was 3D-printed and designed to ensure central fixation. The polarizer and the quarter-wave plate are attached on the fixed arm of the ellipsometer in rotation tables⁵ with an minimal step size of 0.00036° and a maximum angular velocity of $16^\circ/\text{s}$ [20]. The analyzer was mounted in a different rotation table⁶ with a maximum angle velocity of $3000^\circ/\text{s}$ and a minimal step size of 0.00011° on the right arm of the ellipsometer [21].

There are two additional optical components, a polarizer and a quarter-wave plate, which are mounted on the fixed arm (cf. figure 4.1.1 in green font). Their function is explained in section 4.3.3. These two components are attached in manually rotatable rotation tables⁷ because their angle must be adjust only once.

In the setup Glan-Thompson polarizers⁸ with a wavelength range of 350-2700 nm [22] and an achromatic quarter-wave plate⁹ with a wavelength range of 400 - 800 nm [23] are used. The laser¹⁰ and connected monochromator¹¹ allow measurements with different wavelengths in the visible range. The intensity is measured with a photodiode¹² which is connected to a picoammeter¹³. Since the measurements are not performed in a completely dark room and there can be light from other sources than the laser, multiple precautions were taken to reduce the background. A bandpass filter¹⁴ was installed in front of the photodiode and additionally a 3D printed box with a hole was placed over both in order to cover them. For the bandpass 635 nm was selected as transmission wavelength because at this point the laser has a high power density and it is in the wavelength range of the optical components.

4.2 Alignment and cleaning

Two important steps that must be taken into account before any measurement are the alignment of the setup and the cleaning of the optical components.

During the construction of the ellipsometer attention was paid that the individual components were aligned with each other, for example that the center of the hexapod matches with the center of the two rotation tables. The base plate was also balanced with a precision spirit level before and after the assembly of the components. The balancing must be repeated when the construction has been moved.

⁴Standa 8MR151 - Motorized Rotation Stage

⁵PI M-060.DG

⁶PI V-610.998061

⁷Thorlabs RSP1D/M

⁸B.Halle Nachfl. GmbH PGT 3.05

⁹Thorlabs AQWP05M-600

¹⁰NKT Photonics SuperK Compact Supercontinuum Laser

¹¹NKT Photonics LLTF Tunable High Contrast Filter

¹²Hamamatsu S2281

¹³Keithley 6482

¹⁴Thorlabs FL05635-10

Moreover, before each measurement the optical components were cleaned and aligned. Depending on the amount of surface contamination on the optics, different cleaning methods are useful. The methods described in [24] were chosen for cleaning. If the optics are only dusty, a bellows or an air-pressure spray is sufficient to clean them. If the contamination is more severe, the optical component must first be freed from dust and then cleaned with a lens paper and ethanol. Gloves should be worn during cleaning to prevent contamination caused by the hands. In addition, when cleaning with lens paper, attention should be paid to not scratch the surface.

While aligning the optical components to the laser beam, care was taken to ensure that the laser beam passes through the center of the optical components. The resulting back reflection by the optical components was adjusted to be as parallel as possible to the incident beam.

4.3 Characterization

Before an ellipsometry measurement can be performed, the ellipsometer has to be characterized. For the characterization the optical components, polarizer, analyzer and quarter-wave plate, are specified in relation to each other. This is performed because during the installation of the optical components in the mounts and on the rotation tables a shift between the optical axis of the component and the 0° angle of the rotation table may have occurred. For these measurements, the polarizer which is mounted in the manually rotatable rotation table was chosen as reference polarizer. All components are characterized in relation to it.

Besides the characterization of the optical components, the polarization of the laser has to be determined. As described in section 3.5 the laser light is assumed to be unpolarized light, whereas in reality, the majority of lasers has a polarization. In addition, the angle of incidence of the laser on the sample must be defined.

4.3.1 Polarizer and analyzer

First of all, the polarizer and the analyzer which are mounted on the motorized rotation tables were characterized. To do the characterization measurement, the setup which is illustrated in figure 4.3.1 was used.

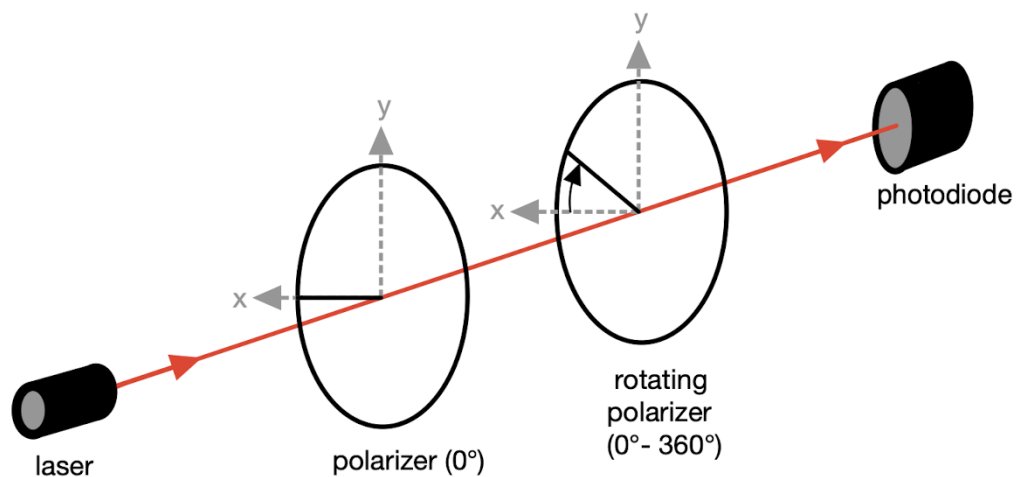


Figure 4.3.1: Setup of the characterization measurement of the polarizer.

The first polarizer is the reference polarizer and is at an angle of 0° . Behind the reference polarizer, the analyzer or polarizer to be investigated are placed. In the following, the latter is referred as

second polarizer. During the measurement the rotation table of the second polarizer was rotated from 0° to 360° in 1° steps and for each step the intensity was measured. With the intensity curve, the shift between the rotation table angle and the polarizer axis can be determined. It was expected that the intensity reaches its maximum when both polarizer axes are parallel to each other. This should be the case for polarizer angles of 0° , 180° and 360° of the second polarizer. Exactly the opposite is expected when the polarizer is at the angles 90° and 270° , where the intensity should reach its minimum or rather zero. This is the case because the two polarizer axes are now perpendicular to each other. Thus, polarized light from the reference polarizer is extinguished because of the second polarizer. The results for the polarizer and analyzer characteristic measurement are shown in figure 4.3.2. The measured intensity was fitted with Malus's Law [15]

$$I = I_0 \cos^2(\alpha + b) + c, \quad (4.3.1)$$

where I_0 describes the initial intensity of the beam before it transmits through the polarizer, α is the angle of the second polarizer, b describes the shift of the polarizer to the rotation table and c the shift because of the background. With this fit, the angle of the second polarizer, where the intensity reach its maximum, can be obtained.

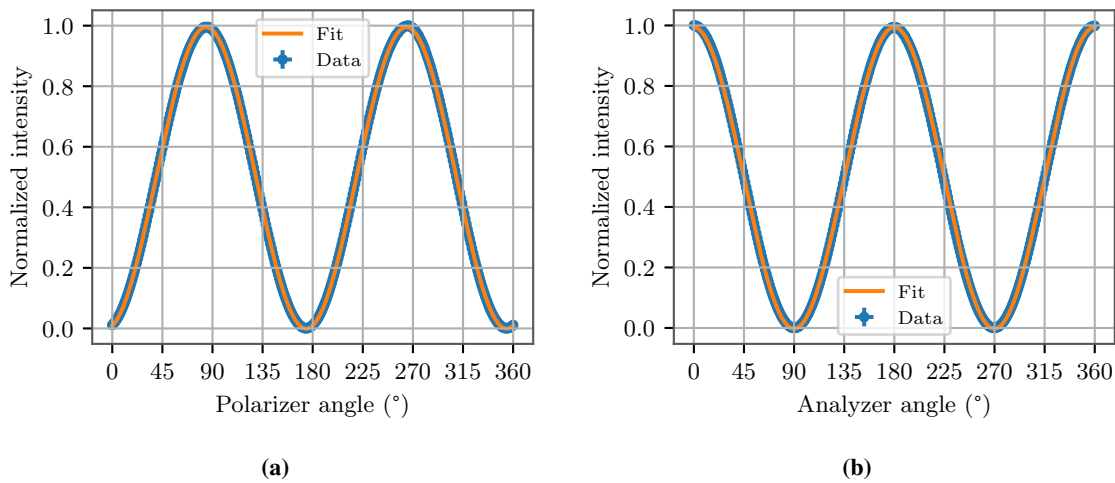


Figure 4.3.2: Characterization measurements for (a) the polarizer and (b) the analyzer. The maximum intensity is normalized to 1.

The measurement with the polarizer (cf. figure 4.3.2 (a)) shows that there is a large shift between the polarizer axis and the 0° of the rotation table because the maximum is at $(84.19 \pm 0.01)^\circ$ and not at 0° as expected. This displacement is too large to result only from mounting the optic in the mount to the rotation table. Other possibilities could be that the marking of the polarizer axis on the optics housing is incorrect or that the optics have been incorrectly built into the housing.

For the analyzer measurement (cf. figure 4.3.2 (b)) it can be seen that the maximum of the intensity is near 0° . The shift is $(0.60 \pm 0.02)^\circ$ and probably results from installing the optic in its mount.

The shifts of the polarizer and analyzer axis to the axis of the rotation table must be taken into account for the further measurements and were corrected in the control program for the rotation tables.

In both measurements, the minimum intensity was expected to be in the background region because in the minimum the second polarizer theoretically does not transmit the light from the first polarizer since both polarizer axes are perpendicular to each other. This can be observed in both measurements. The minimum of the normalized intensity in the polarizer measurement is $(6.3 \pm 0.4) \cdot 10^{-4}$ and the

background is $(6.0 \pm 0.4) \cdot 10^{-4}$ and for the analyzer measurement the minimum is $(1.3 \pm 0.3) \cdot 10^{-4}$ and the background is $(1.1 \pm 0.4) \cdot 10^{-4}$.

4.3.2 Quarter-wave plate

After the characterization of the polarizers the two quarter-wave plates were characterized. In this measurement, two polarizers were placed perpendicular to each other with a quarter-wave plate in between which is analyzed in the following (cf. fig. 4.3.3).

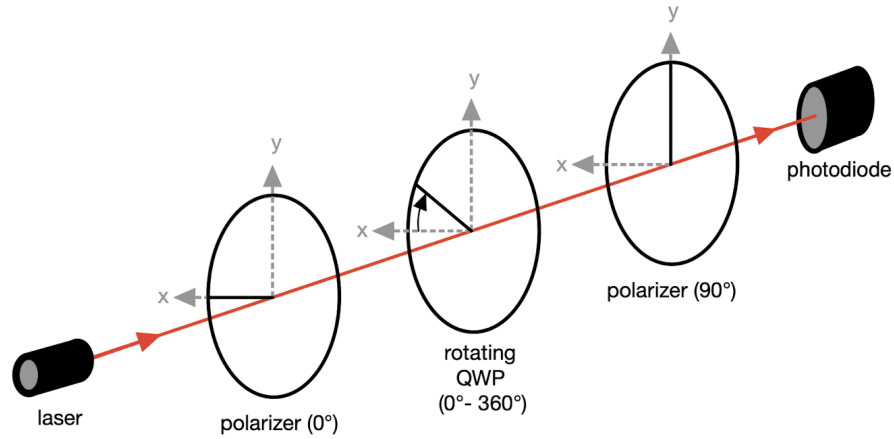


Figure 4.3.3: Setup of the characterization measurement of the quarter-wave plate (QWP).

The first polarizer in this setup is the reference polarizer at an angle of 0° . The second polarizer is characterized in section 4.3.1 and set to 90° . For the intensity measurement, the rotation table of the quarter-wave plate was rotated from 0° to 360° in 1° steps for the motorized rotation table and in 4° for the manually rotatable rotation table. The shift between the fast axis of the quarter-wave plate and the 0° of the rotation table can be again determined by the intensity curve.

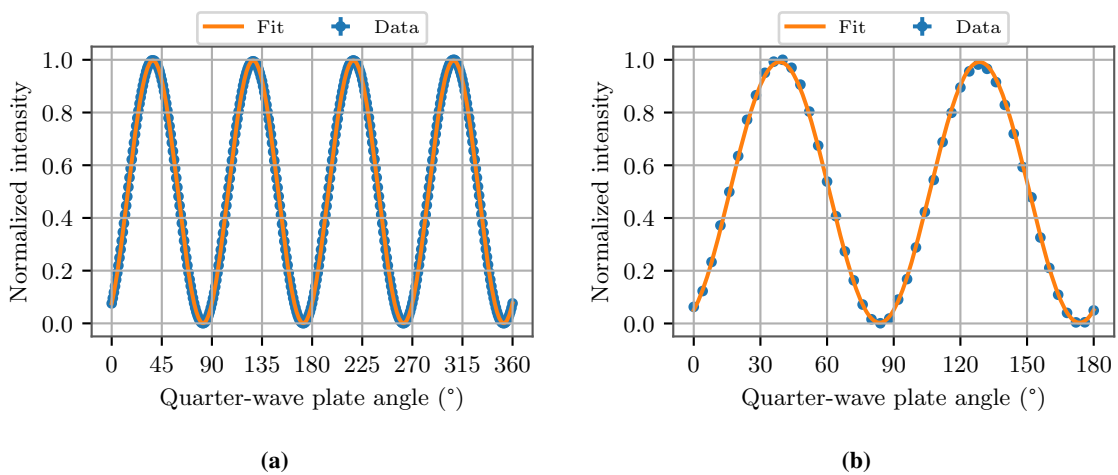


Figure 4.3.4: Characterization measurement for two quarter-wave plates, (a) one mounted in a motorized rotation table and (b) the other one in a manually rotatable rotation table.

The maximum of intensity is expected when the angle of the quarter-wave plate is shifted by 45° or by -45° to one of the polarizer axes. From this results that at the quarter-wave plate angles of 45° ,

135° , 225° and 315° a maximum is expected. This is the case because the quarter-wave plate shifts the phase by 90° and thus the polarized light from the reference polarizer is parallel to the polarizer axis of the second polarizer. But if the fast axis of the quarter-wave plate is parallel to one of the polarizer axes, the intensity is at its minimum.

In figure 4.3.4 the intensity measurement for both quarter-wave plates is shown. The intensity was fitted with the following equation

$$I = a \cdot \sin(2(\alpha - b))^2 + c, \quad (4.3.2)$$

where α is the quarter-wave plate angle, a a coefficient, b the shift of quarter-wave plate to the rotation table and c the shift due to the background. It can be seen that in both measurements the position of the maximum intensity features an offset by some degree from the expected 45° . For the quarter-wave plate in the motorized rotation table the shift is $(-7.98 \pm 0.01)^\circ$ and for the other quarter-wave plate it is $(-6.36 \pm 0.06)^\circ$. These shifts are a little bit larger than in the expected range between -4° to 4° . A reason for the larger shift besides the mounting in the rotation table can be that the quarter-wave plate itself could have a shift to its axis marked on its housing.

The minimum intensity of the quarter-wave plate should be within the order of magnitude of the background and this is the case for both measurements. For the quarter-wave plate in the motorized rotation table the minimum normalized intensity is at $(4.3 \pm 0.7) \cdot 10^{-4}$ and the normalized background is at $(2.2 \pm 0.7) \cdot 10^{-4}$. For the other quarter-wave plate the normalized intensity amounts to $(8.5 \pm 0.2) \cdot 10^{-4}$ and the normalized background to $(2.0 \pm 0.2) \cdot 10^{-4}$.

4.3.3 Polarization of the laser

As described in section 3.6 a rotating quarter-wave plate stokes polarimeter can be used to determine the polarization of the used laser. The setup of such a polarimeter is illustrated in figure 4.3.5.

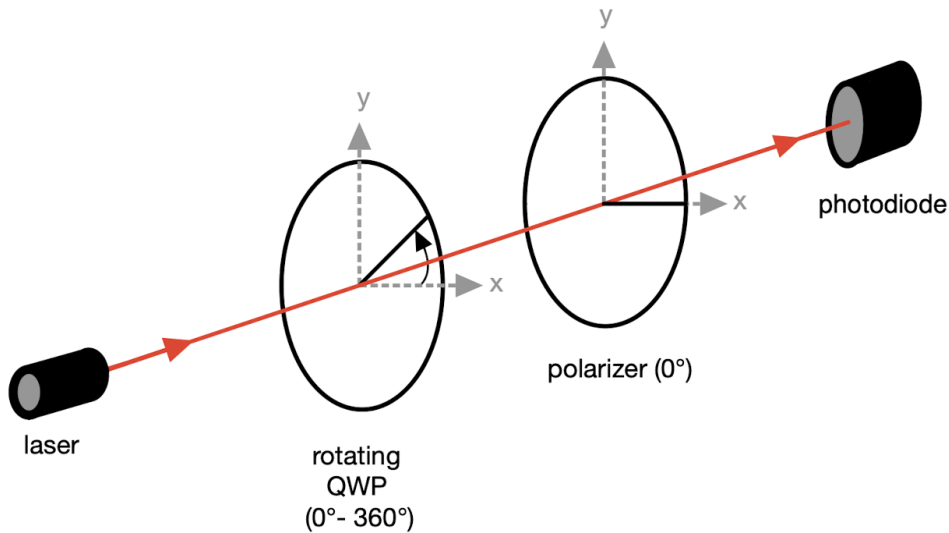


Figure 4.3.5: Setup of a rotating quarter-wave plate stokes polarimeter.

For the setup the quarter-wave plate, which is mounted in the motorized rotation table, and the reference polarizer were used. The quarter-wave plate was rotated from 0° to 360° in 1° steps during the intensity measurement while the polarizer staid at 0° . Figure 4.3.6 shows the measured intensity which was fitted with equation 3.6.2 (cf. section 3.6).

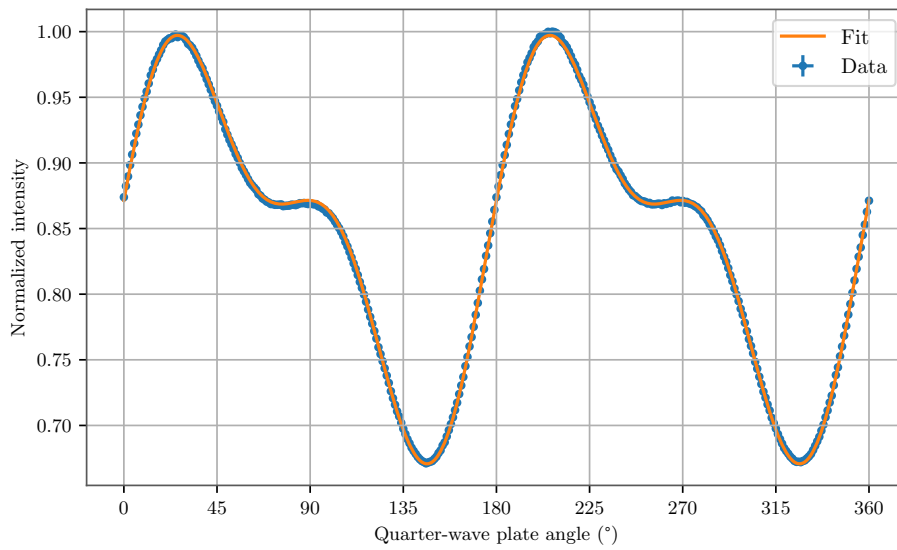


Figure 4.3.6: The intensity curve measured with the rotating quarter-wave plate stokes polarimeter plotted against the angle of the quarter-wave plate

In comparison with the illustrations in figure 3.6.2, it can be seen that the laser is elliptical polarized. A more accurate statement can be made with the Stokes parameters determined by the fit. The Stokes parameters are listed in table 4.3.1.

Table 4.3.1: Stokes parameters of the laser determined by the fit.

| Stokes parameter | S_0 | S_1 | S_2 | S_3 |
|------------------|---------------------|---------------------|---------------------|----------------------|
| Fit | 1.6426 ± 0.0003 | 0.1003 ± 0.0004 | 0.2423 ± 0.0005 | -0.2490 ± 0.0002 |

In this case the laser is partially polarized light because S_0^2 is greater than the sum of the squares of the Stokes parameters $S_1^2 + S_2^2 + S_3^2 = 0.1308 \pm 0.0002$ (cf. section 3.3).

In the theoretical introduction in section 3.5 the light of the laser is assumed to be unpolarized. To remove the polarization of the laser, the light is transformed into circular polarized light before it passes the polarizer. To obtain circular polarized light, the light has to go first through a polarizer and then through a quarter-wave plate, where its fast axis is shifted by 45° to the polarizer axis. For this reason, the two additional components mentioned in section 4.1 are needed.

To control if the light is circular polarized after going through the two components a second polarizer was set behind the components. If the second polarizer rotates from 0° to 360° and the intensity is measured, a constant intensity is expected. During the measurement it could be observed that the intensity is still angle dependent. Because of this the aforementioned measurement was repeated with different quarter-wave plate angles in a range from 42.5° to 48° in 0.5° steps to acquire the quarter-wave plate angle where the intensity change the least.

In figure 4.3.7 (a) the measurement results for a quarter-wave plate angle of 45.5° is shown and it should be noted that the intensity is angle dependent as mentioned before. In figure 4.3.7 (b) the difference between the intensity maximum and minimum for the different quarter-wave plate angles were plotted. The data were fitted with a parabola to get the quarter-wave plate angle where the intensity varies the least. The minimum variation of $(7.460 \pm 0.001)\%$ is located at an angle of

$(45.43 \pm 0.01)^\circ$. Due to the accuracy of the rotation table an angle of $(45.5 \pm 0.1)^\circ$ was set for the next measurements.

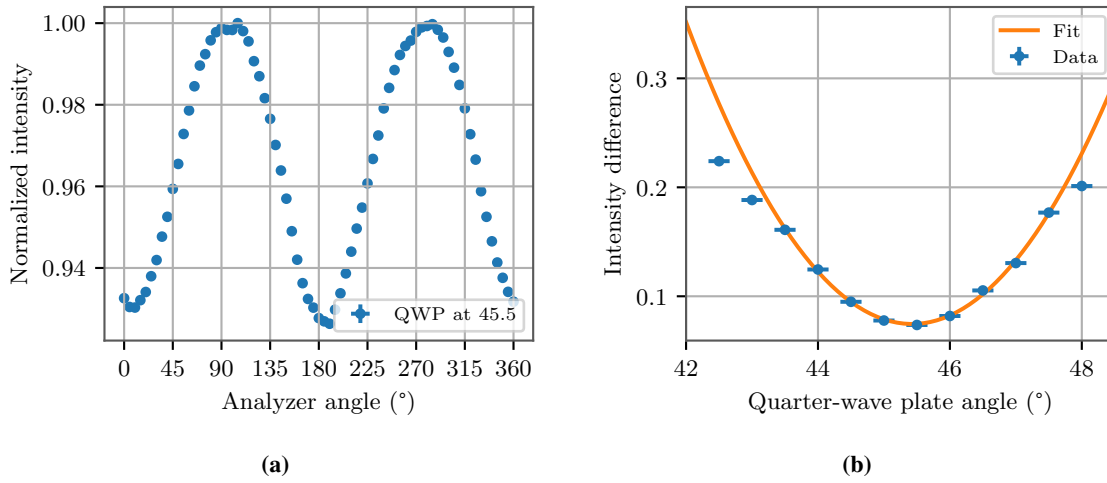


Figure 4.3.7: (a) Measured intensity curve for a quarter-wave plate angle of 45.5° . (b) The intensity difference between the minima and maxima of the intensity curve plotted for all measured quarter-wave plate angles, fitted with a parabola.

4.3.4 Incident angle

Another important parameter which has to be well-defined for an ellipsometry measurement, is the incident angle of the laser beam on the sample. The accuracy of the incident angle should be more accurate than 0.1° . To determine the incident angle a plate with three pinholes of diameter d of 0.7 mm, 0.6 mm and 0.5 mm was manufactured. The setup for the determination of the angle of incidence is illustrated in figure 4.3.8.

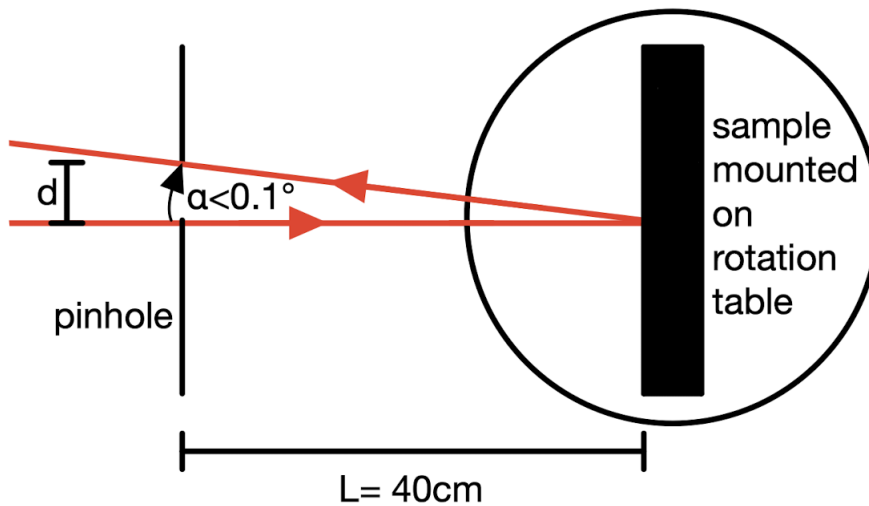


Figure 4.3.8: Illustration of the setup for the determination of the incident angle.

First, the sample was mounted on the rotation table and the plate with the pinholes was added to the beam path with a distance of $L = (40.0 \pm 0.1)\text{ cm}$ from the sample. For this purpose, the pinhole with a diameter $d = 0.7\text{ mm}$ was used first. Then the sample was rotated with the rotation table until the reflected beam of the sample is guided back through the pinhole. This was repeated for the two

smaller pinholes. Afterwards, it was possible to determine the maximum possible angle α between the incoming and the reflected beam. The resulting relationship between the distance L , the pinhole diameter d and the angle α

$$\tan(\alpha) = \frac{d}{L} \quad (4.3.3)$$

was used for this purpose. For a pinhole diameter of $d = 0.5 \text{ mm}$ α is $(0.07 \pm 0.01)^\circ$ which satisfies the desired accuracy of the angle of incidence. It should be noted that this procedure must be repeated for each sample because not all of the samples can be mounted exactly the same way on the rotation table.

5 Ellipsometry measurements

In this chapter the three analyzed samples are introduced and the results for two different ellipsometry methods, null ellipsometry and rotating analyzer ellipsometry, are shown. The goal is to reproduce the known properties of the samples. For each angle of incidence at the sample the two methods were measured in direct succession such that both measurements took place under the same conditions and thus the results are comparable. All measurements were performed using a laser with a wavelength of 635 nm and in a dark laboratory tempered to 18 °C. Before a measurement could be performed, the laser was turned on for two hours, after which the laser intensity output is constant.

5.1 Samples

Three samples with different materials and layer thicknesses were analyzed to determine the performance of the ellipsometer. All samples consist of a three layer system for which the refractive index and the thickness of the layer to be examined are known.

The first sample which was analyzed was a compact disc (CD). The CD was chosen because of its optical properties which are well known. The structure of a CD is illustrated in figure 5.1.1.

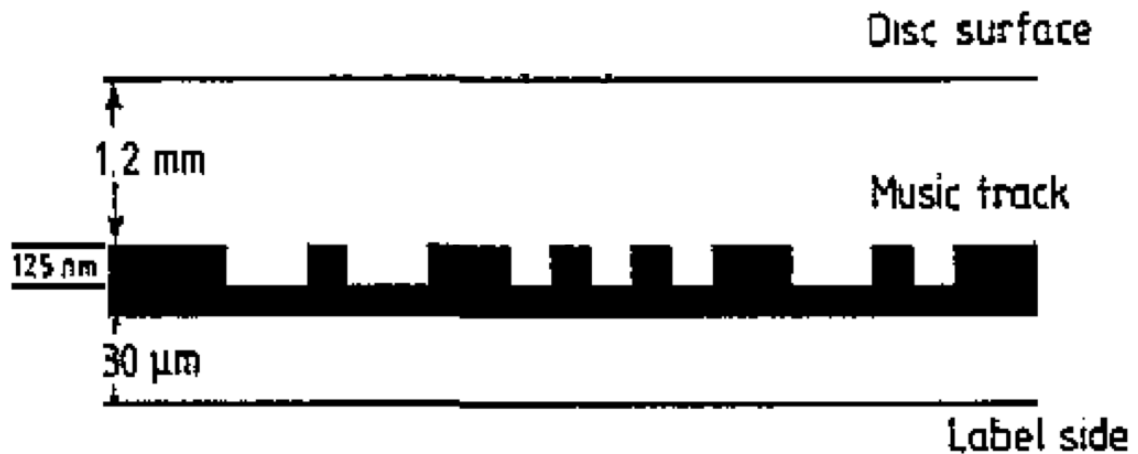


Figure 5.1.1: The illustrated layer system of the CD sample. Figure taken from [25] and modified.

It consists of a 1.2 mm thick polycarbonate layer which has a complex refractive index of $N_{poly} = 1.5803 + 0i$ [26] at a wavelength of 635 nm. Underneath this layer is a layer of aluminum with a complex refractive index of $N_{Al} = 1.4622 + 7.5592i$ [27] at 635 nm in which the information of the CD has been stamped. Since it is not possible to recognize where a pit or a land is located, the measurement was performed in the blank part. In this part the CD does not contain any information and therefore the CD in this part does not have any pits and is therefore flat. After the aluminum layer comes a thin varnish and the label of the CD [25]. These two layers are not important for the measurement because aluminum is highly reflective and can therefore be assumed as the substrate, whereas the polycarbonate is the layer in the three layer system.

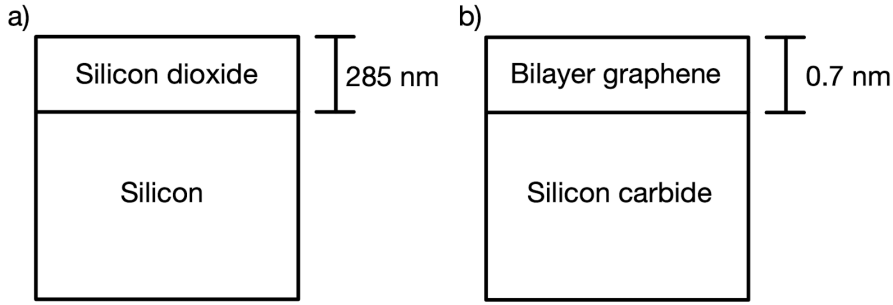


Figure 5.1.2: The illustrated layer system of the **a)** silicon dioxide layer on silicon sample and of the **b)** bilayer graphene layer on silicon carbide sample. The illustration is not true to scale.

The second sample¹⁵ analyzed was a silicon dioxide (SiO_2) layer on a silicon crystal (Si) (cf. figure 5.1.2 **a)**). The layer thickness of the silicon dioxide layer is 285 nm and has a complex refractive index of $1.457 + 0i$ at 635 nm. The complex refractive index for the silicon substrate is $3.877 + 0.019i$ at 635 nm [28]. The two refractive indices were determined from the respective dielectric function ϵ of SiO_2 and Si. The dielectric function consists of

$$\epsilon = \epsilon_1 + i\epsilon_2, \quad (5.1.1)$$

where ϵ_1 is the real part and ϵ_2 the imaginary part of the dielectric function. ϵ_1 and ϵ_2 are related by the following equations

$$\epsilon_1 = n^2 - k^2, \quad \epsilon_2 = 2nk \quad (5.1.2)$$

to the refractive index n and to the extinction coefficient k . From this relationship the following equations are obtained for the refractive index n and the extinction coefficient k [15]

$$n = \sqrt{\epsilon_1 + \frac{\sqrt{\epsilon_1^2 + \epsilon_2^2}}{2}}, \quad k = \sqrt{\epsilon_1 - \frac{\sqrt{\epsilon_1^2 + \epsilon_2^2}}{2}}. \quad (5.1.3)$$

The third sample¹⁵ is bilayer graphene on a silicon carbide (SiC) substrate (cf. figure 5.1.2 **b)**). The bilayer graphene is (0.7 ± 0.4) nm [28] thick and has a refractive index of $n = 2.55 \pm 0.01$ and an extinction coefficient of $k = 1.71 \pm 0.01$ [29] at 635 nm. Silicon carbide has a refractive index of $n = 2.6336$ [28] at 635 nm. As for the second sample the refractive indices of the substrate were determined with the dielectric function.

5.2 Null Ellipsometry

The samples were first analyzed using null ellipsometry. The setup for this method was build as shown in figure 3.5.2. The aim of the null ellipsometry is to determine the angle of the polarizer P and the angle of the analyzer A where the intensity reaches its minimum (cf. section 3.5.1). To obtain these two angles, a full scan from $P = 0^\circ - 360^\circ$ and $A = 0^\circ - 360^\circ$ in 5° steps for each combination with a quarter-wave plate at an angle of 45° was measured. The full scan thereby serves to identify

¹⁵Kindly provided by U. Wurstbauer

the region where the minimum is located. Afterwards, this region was measured again with a minimum scan. A minimum scan is the same measurement as before but in a smaller region with smaller step size. As several minima can be detected in a full scan, an arbitrary region was chosen for the minimum scan. To get the angles of the polarizer P and analyzer A at the intensity minimum it was fitted with a bivariate normal distribution.

After the values of P and A were determined, a Python program was used to calculate the complex refractive index N and the thickness d of the examined layer. The Python program was developed by Fausto Frisenna during a collaboration with the DFG Research Training Group 2149¹⁶. It calculates the two ellipsometry parameters ψ and Δ from the polarizer and analyzer angle using equations 3.5.3 and 3.5.4. With the two ellipsometry parameters the ρ parameter is calculated using equation 3.4.11. Apart from the calculation with the ellipsometry parameters, ρ can also be determined by the reflection coefficients for s-polarized r_s and p-polarized r_p light. This ρ calculated via the reflection coefficients is described in the following by $\tilde{\rho}$. In order to calculate $\tilde{\rho}$ or the reflection coefficients, the refractive indices of the ambient, the substrate and the layer as well as the thickness of the layer are required. Because the refractive indices of the ambient and the substrate are known, they are predefined in the Python program. The complex refractive index N and the thickness d of the layer are defined as variables within a limited value range. If the extinction coefficient k for the investigated sample is zero, this coefficient was predefined and only the refractive index n and the thickness d were defined as variables.

In order to be able to determine these variables, the Python program minimizes the difference between ρ and $\tilde{\rho}$, in other words the difference between measurement and theory, with the help of a minimization function by calculating the variables combination with the smallest difference. Then this combination of variables gives the complex refractive index N and the thickness d of the analyzed layer.

Several uncertainties must be taken into account when calculating the complex refractive index and the thickness of the layer. Besides the general background in the laboratory, which is already considered before the fits of the measured data, uncertainties like the wavelength range of the laser, the accuracy of the rotation table and the uncertainty of the angle of incidence are also considered. Therefore, the minimization is performed several times by sampling these parameters from a gaussian of standard deviation equaling their uncertainty. The resulting complex refractive index N and the resulting thickness d are the mean value of all performed minimizations.

5.2.1 Compact Disc

The Compact Disc (CD) sample was analyzed with the null ellipsometry for different incident angles in a range of 30° to 60° in 5° steps. As mentioned before, a full scan and a successive minimum scan were done for each incident angle. The full scans for the incident angles are shown in figure 5.2.1.

Since the angle of incidence has an influence on the polarization change of the light due to the reflection on the sample, it is expected that the pattern of the full scan differs or that the minima shift. These assumptions can also be seen in the full scans. By comparing the full scans of all incident angles, it can be recognized that the pattern changes from a rather dotted pattern at an incident angle of 30° to a rather diagonally striped pattern with a slightly dotted pattern at 40° angle of incidence to a, once again, rather dotted pattern with diagonal stripes at an incident angle of 55° .

¹⁶<https://www.uni-muenster.de/Physik.GRK2149/index.html>

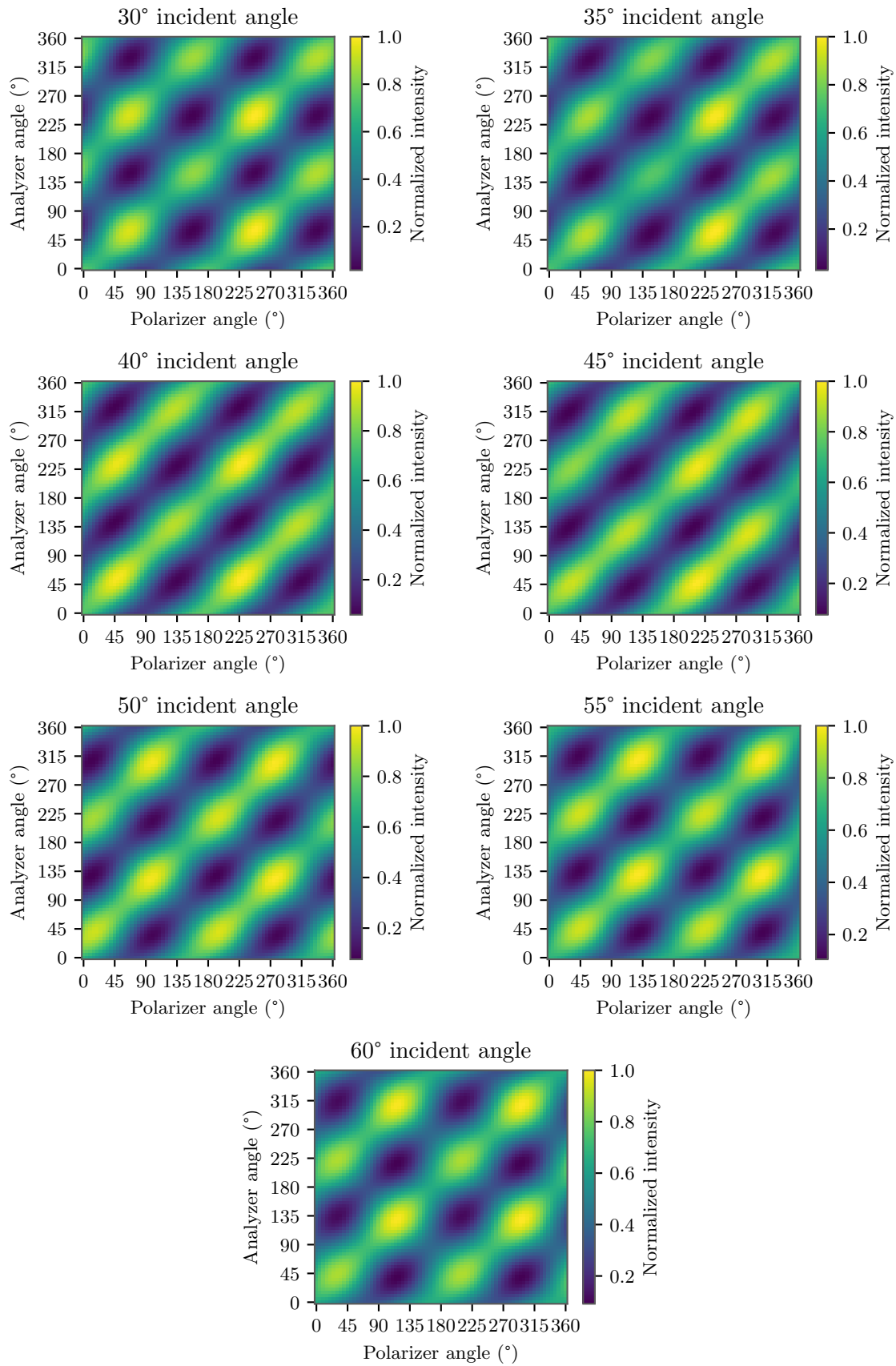


Figure 5.2.1: The full scans for the null ellipsometry measurement of the CD sample at incident angles of 30°, 35°, 40°, 45°, 50°, 55° and 60°.

Thereby, it can also be seen that the minima shift diagonally to the lower left respectively to smaller polarizer and analyzer angles. But at an incident angle of 55° , it is shown that the minima are shifting back to the upper right and then for an angle of incidence of 60° they shift again to the lower left. The expectation was that the pattern changes in a certain way for higher incidence angles, for example that the minima shift in the same direction, here to the lower left. This is not true for an incident angle of 55° . A reason for this could be that the measurements for the incident angles of 55° and 60° were repeated due to an error in the first measurements and because of this it could have happened that not the exact same position on the CD sample was measured. Therefore, it is difficult to compare the data. However, if only these two measurements are considered, the shift of the minimum to the lower left can be seen again.

All full scans have in common that the pattern repeats itself every 180° no matter which axis of the scan is considered. This is expected because the position of the polarization axis of the polarizer as well as the analyzer is repeated every 180° . But it can also be seen that the intensity of the maxima varies. This can have several causes. On the one hand, the back reflection of the optical components may not be absolutely parallel to the incident beam which can lead to intensity fluctuations when rotating the rotation stages. On the other hand, the beam can move minimally due to the rotation of the optical components and thus a different position on the sample is measured which can also lead to intensity fluctuations. From these observations follows that, as expected, the angle of incidence has an effect on the polarization of the light and thus the patterns of the scans and the locations of the minima change for different angles of incidence.

After each full scan a minimum scan was measured. One example of a minimum scan at an incident angle of 45° is shown in figure 5.2.2.

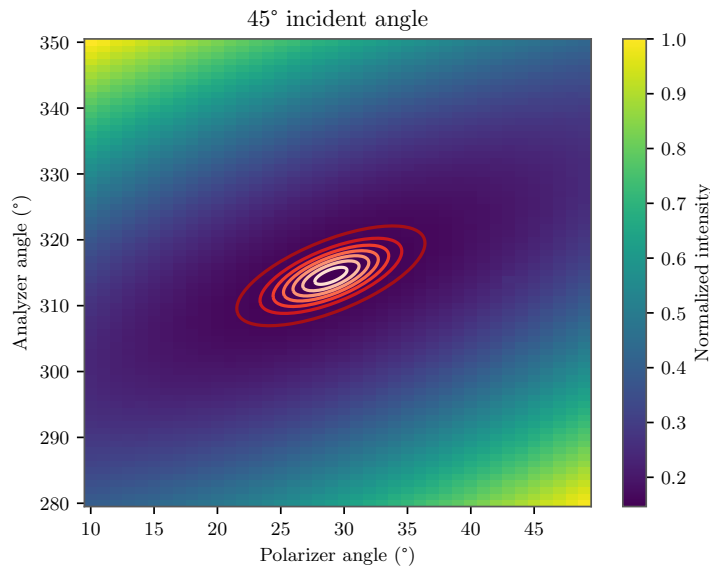


Figure 5.2.2: The minimum scan for the null ellipsometry of the CD sample at an incident angle of 45° . The red contour lines indicate the fit with a bivariate normal distribution.

The red contour lines indicate the fit with a bivariate normal distribution. The polarizer angle and analyzer angle at the minimum given by the fit are listed in table 5.2.1 for all measured incident angles. Since the pattern of the measurements for the incident angles 30° to 50° look similar, it was always tried to measure the same minimum. This was not possible for the measurement at an incident angle of 50° , so for this measurement another minimum was scanned. It can be seen that the measured

minimum shifts diagonal to the bottom left the higher the incident angle is. This was expected because as described before, the change of the incident angle results in a shift of the minimum. This can also be seen for the incident angle of 55° and of 60° . Here the measured minimum shifts to the lower left, since these measurements were redone as mentioned above.

Table 5.2.1: Values of the polarizer angle P and of the analyzer A for different angles of incidence at a minimum intensity resulting from the minimum scans of the null ellipsometry for the CD sample.

| Incident angle | Polarizer angle P | Analyzer angle A |
|--------------------------|---------------------|---------------------|
| $(30.00 \pm 0.07)^\circ$ | $(69 \pm 2)^\circ$ | $(331 \pm 2)^\circ$ |
| $(35.00 \pm 0.07)^\circ$ | $(57 \pm 1)^\circ$ | $(326 \pm 1)^\circ$ |
| $(40.00 \pm 0.07)^\circ$ | $(46 \pm 2)^\circ$ | $(323 \pm 2)^\circ$ |
| $(45.00 \pm 0.07)^\circ$ | $(29 \pm 3)^\circ$ | $(315 \pm 4)^\circ$ |
| $(50.00 \pm 0.07)^\circ$ | $(100 \pm 1)^\circ$ | $(35 \pm 1)^\circ$ |
| $(55.00 \pm 0.07)^\circ$ | $(130 \pm 2)^\circ$ | $(40 \pm 2)^\circ$ |
| $(60.00 \pm 0.07)^\circ$ | $(115 \pm 2)^\circ$ | $(35 \pm 2)^\circ$ |

With the angles shown in table 5.2.1 and the help of the previously described analysis program, the complex refractive index N and the thickness d of the polycarbonate layer can be determined. Since the extinction coefficient of polycarbonate is $k = 0$, it was not included as a variable but as a parameter in the analysis program.

The values calculated from the analysis program for the refractive index n and the thickness d of the polycarbonate layer are shown in table 5.2.2 for all incident angles. As explained in section 5.1, a complex refractive index of $N = 1.5803 + 0i$ at 635 nm and a thickness of 1.2 mm are expected. The determined refractive indices and thicknesses of all incident angles agree with the expected properties of the layer.

Table 5.2.2: Values of the refractive index n and of the layer thickness d of the polycarbonate layer of the CD sample for different angles of incidence resulting from the null ellipsometry.

| Incident angle | Refractive index n | Layer thickness d |
|----------------|----------------------|------------------------|
| 30.00° | 1.581 ± 0.004 | (1.21 ± 0.03) mm |
| 35.00° | 1.580 ± 0.003 | (1.20 ± 0.01) mm |
| 40.00° | 1.583 ± 0.008 | (1.197 ± 0.009) mm |
| 45.00° | 1.582 ± 0.001 | (1.20 ± 0.02) mm |
| 50.00° | 1.581 ± 0.004 | (1.199 ± 0.003) mm |
| 55.00° | 1.580 ± 0.001 | (1.200 ± 0.001) mm |
| 60.00° | 1.581 ± 0.003 | (1.199 ± 0.003) mm |
| expected value | 1.5803 | 1.2 mm |

Nevertheless, it can be observed that the uncertainties of the different measurements vary strongly but the values are in the same order of magnitude. This may be due to the evaluation program since the average of all minimizations is taken as the result and the standard deviation as the uncertainty. Figure 5.2.3 shows the calculated refractive index of the individual minimizations as well as the average and the standard deviation for the angles of incidence of 35° and 55° . It can be observed that there are significantly more strong deviations from the average value for an incident angle of 35° than for the minimizations at 55° . Therefore, the uncertainty of the refractive index for the incident angle of 35° is larger than for 55° . This effect, that some measurements have clearly more stronger deviations than other is not only the case in this measurement but is also evident in all following measurements.

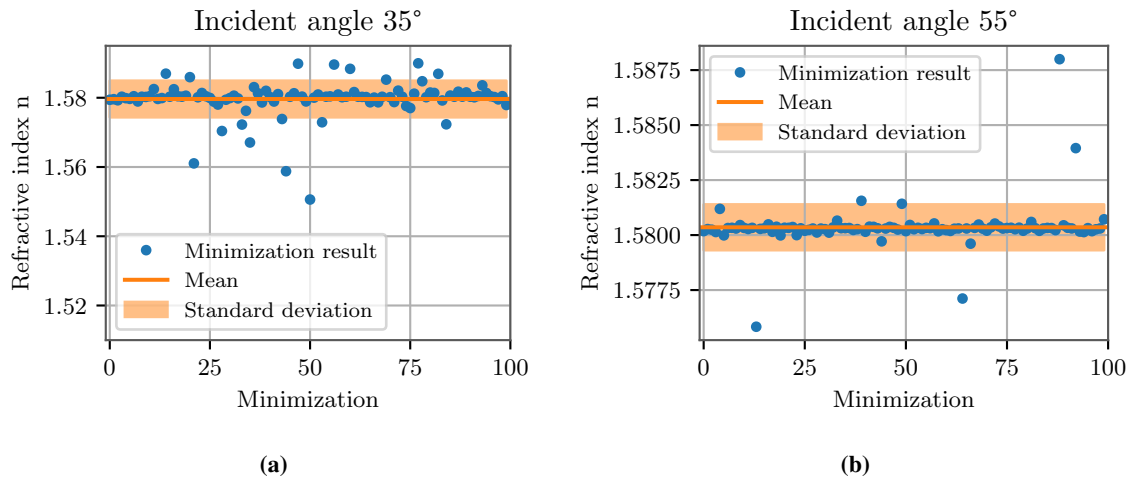


Figure 5.2.3: The calculated refractive index of the individual minimizations as well as the average and the standard deviation of them for the angles of incidence of 35° and 55° .

5.2.2 Silicon dioxide/ silicone sample

The silicon dioxide (SiO_2) / silicone (Si) sample was analyzed at one incident angle, namely at 45° . Since the sample is very small, it was mounted on a microscope slide that could be more easily fixed in the setup. As with the CD sample, first a full scan was performed to determine the location of the minima. The full scan is shown in figure 5.2.4.

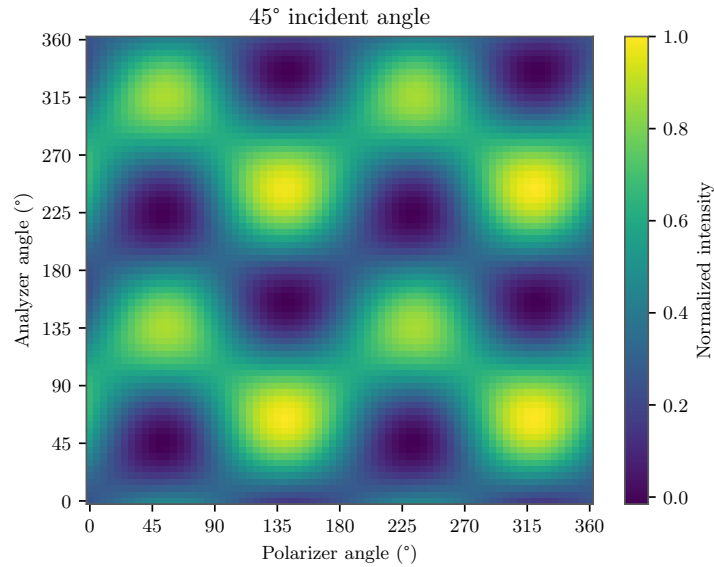


Figure 5.2.4: The full scan of the silicon dioxide / silicon sample for the null ellipsometry at an incident angle of 45° .

It can be seen that the pattern repeats as expected every 180° and also that the intensity varies between the different maxima. These variations can occur for back reflections in the setup which influence the intensity measurements at different polarizer and analyzer angles. For the minimum scan the angles region from 0° to 90° for the polarizer and analyzer was measured in 1° steps.

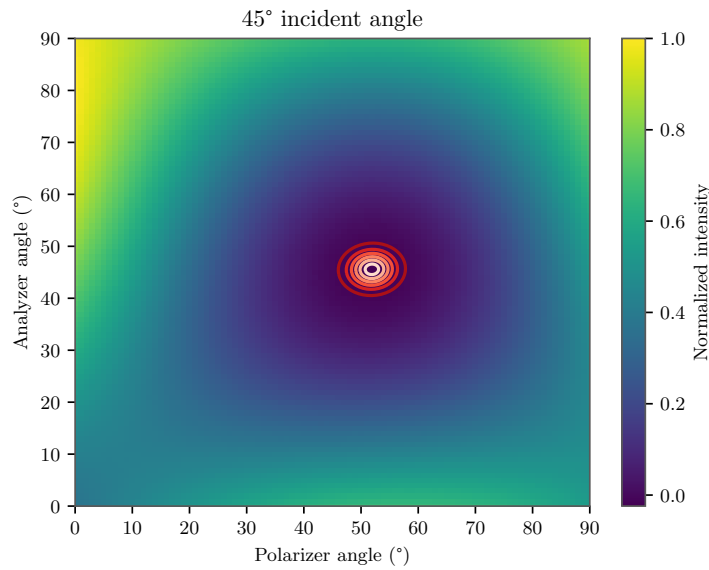


Figure 5.2.5: The minimum scan of the null ellipsometry for the silicon dioxide / silicon sample at an incidence angle of 45° . The red contour lines indicate the fit with a bivariate normal distribution.

The minimum scan and the bivariate normal distribution fit, to get the position of the minimum, are shown in figure 5.2.5. In table 5.2.3 the polarizer and analyzer angle at the minimum and the ellipsometry parameters calculated from them with the equations 3.5.3 and 3.5.4 are listed. In table 5.2.4 the expected and measured values for the refractive index n and the thickness d of the silicon dioxide layer are shown.

Table 5.2.3: Values of the polarizer angle P , of the analyzer A and of the two ellipsometry parameters ψ and Δ for an angle of incidence of 45° at a minimum intensity resulting from the minimum scan of the null ellipsometry for the silicon dioxide / silicon sample.

| Incident angle ($^\circ$) | P ($^\circ$) | A ($^\circ$) | ψ ($^\circ$) | Δ ($^\circ$) |
|-----------------------------|------------------|------------------|---------------------|-----------------------|
| 45.00 ± 0.07 | 52 ± 2 | 46 ± 1 | 45.00 ± 1.49 | 194 ± 4 |

Table 5.2.4: The measured and expected values of the refractive index n and the thickness d measured with the null ellipsometry for the silicon dioxide / silicon sample.

| | n | d (nm) |
|----------------|-----------------|-------------|
| measured value | 1.48 ± 0.07 | 279 ± 7 |
| expected value | 1.457 | 285 |

The refractive index n and the thickness d were calculated with the help of the analysis program described in section 5.2 and the values from table 5.2.3. It can be seen that the measured value of the refractive index is higher and for the thickness the measured value is lower than the expected ones. However, they are still within the uncertainty region of the expected values. The range of the uncertainty of the refractive index does include the expected refractive index and the expected thickness is also in the range of the uncertainty of the measured thickness. However, the uncertainty of the measured thickness is large. The difference between the values may be due to beam deviations of the back reflection because of an imperfect alignment. Another reason could be the thickness of the silicon dioxide layer because in comparison to the analyzed layer of the CD, the thickness is

significantly smaller. Maybe the alignment components before the sample respectively of the beam must be even more precised.

5.2.3 Bilayer graphene / silicon carbide sample

As for the silicon dioxide / silicon sample, the sample with the bilayer graphene on silicon carbide (SiC) was measured at an incident angle of 45° .

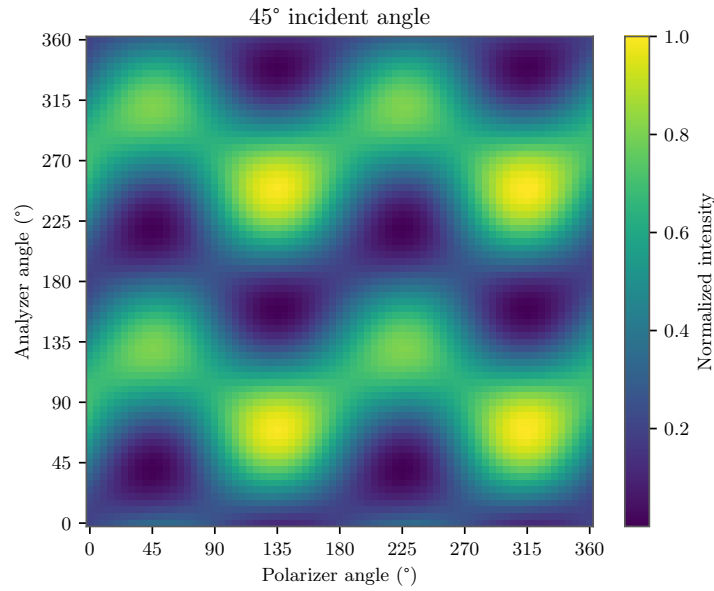


Figure 5.2.6: The full scan for the null ellipsometry of the bilayer graphene / silicon carbide sample measured at an incident angle of 45° .

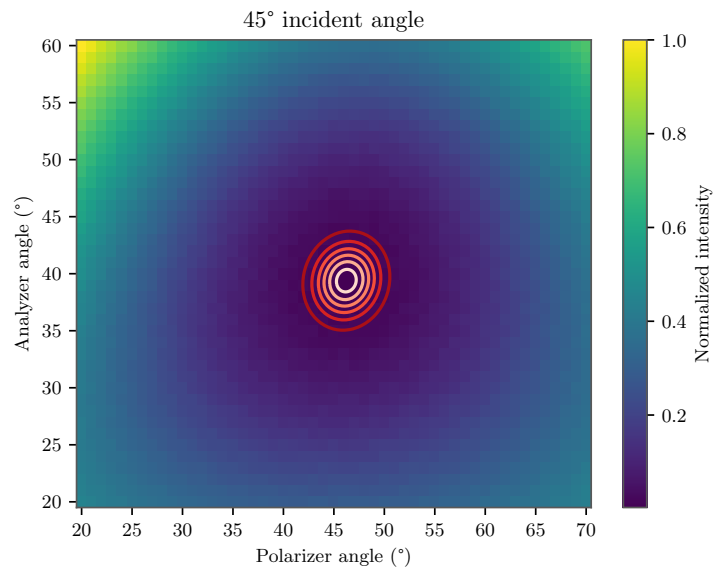


Figure 5.2.7: The minimum scan for the null ellipsometry of the bilayer graphene on silicon carbide sample measured at an incident angle of 45° . The red contour lines indicate the fit with a bivariate normal distribution.

It can be seen in the full scan (cf. figure 5.2.6) that the pattern is repeating every 180° . As with the other samples, the intensity of the maxima varies and is not the same as expected. To analyze the

sample a minimum scan in the polarizer and analyzer region from 30° to 70° with a step size of 1° was performed with the corresponding results shown in figure 5.2.7. With the help of the bivariate normal distribution fit, the angles of the polarizer and analyzer for the position of the minimum shown in table 5.2.5 were determined and the ellipsometry parameters ψ and Δ were calculated from them.

Table 5.2.5: The value of the polarizer angle P , of the analyzer A and of the two ellipsometry parameters ψ and Δ for an angles of incidence of 45° at a minimum intensity resulting from the minimum scan of the null ellipsometry for the bilayer graphene / silicon carbide sample.

| Incident angle ($^\circ$) | P ($^\circ$) | A ($^\circ$) | ψ ($^\circ$) | Δ ($^\circ$) |
|-----------------------------|------------------|------------------|---------------------|-----------------------|
| 45.0 ± 0.7 | 46 ± 2 | 39 ± 2 | 39 ± 2 | 182 ± 4 |

With the values from table 5.2.5 and the analysis program which is explained in section 5.2, the refractive index n , the extinction coefficient k and the thickness d of the bilayer graphene were determined. The results for these parameters and the expected values are listed in table 5.2.6.

Table 5.2.6: The measured and expected values of the refractive index n , the extinction coefficient k and the thickness d measured with the null ellipsometry for the bilayer graphene / silicon carbide sample.

| | n | k | d (nm) |
|----------------|-----------------|-----------------|-----------------|
| measured value | 2.43 ± 0.02 | 1.89 ± 0.03 | 1.26 ± 0.09 |
| expected value | 2.55 ± 0.01 | 1.71 ± 0.01 | 0.7 ± 0.4 |

It can be seen that the measured values are in the assumed range of the expected values but for the refractive index n the expectation is higher and the expected value is not within the uncertainty range. For the extinction coefficient k the calculated value is higher than the expected value and also the expected value is not within the uncertainty range. The calculated thickness d is not in the uncertainty range of the expected value and the value is higher than expected. These difference can be again attributed to beam alignment and back reflections as for the other samples. Another reason could be the step size of the minimum scan that the chosen step size is too large. If a smaller step size is chosen, the minimum can be determined more precisely for more accurate results.

5.3 Rotating Analyzer Ellipsometry

The rotating analyzer ellipsometry was the second method used to analyze the samples. The setup was constructed along the principle illustrated in figure 3.5.3. The setup of the rotating analyzer ellipsometry was build and including a quarter-wave plate.

During the measurements the analyzer was rotated at an angular velocity of $\omega = 11.25 \frac{^\circ}{s}$ and the intensity was recorded. This angular velocity was chosen because at higher velocities the photodiode records too few measurement points and so the data can not be analyzed well later. The quarter-wave plate was set to 0° for all measurements and the polarizer angle was varied. The measurements were performed for polarizer angles in a range of 30° to 60° in 5° steps. The measured intensity curves were fitted with the equation 3.5.7 and with the help of the fit the ellipsometry parameters ψ and Δ were determined. Furthermore, with these parameters the complex refractive index N and the film thickness d were calculated using the analysis program described in section 5.2. The difference to the analysis program is here that ψ and Δ are directly read into the program to calculate ρ and is not calculated first as in the null ellipsometry.

5.3.1 Compact disc

The Compact Disc (CD) sample was not only measured for different polarizer angles but also for different incident angles as in the null ellipsometry.

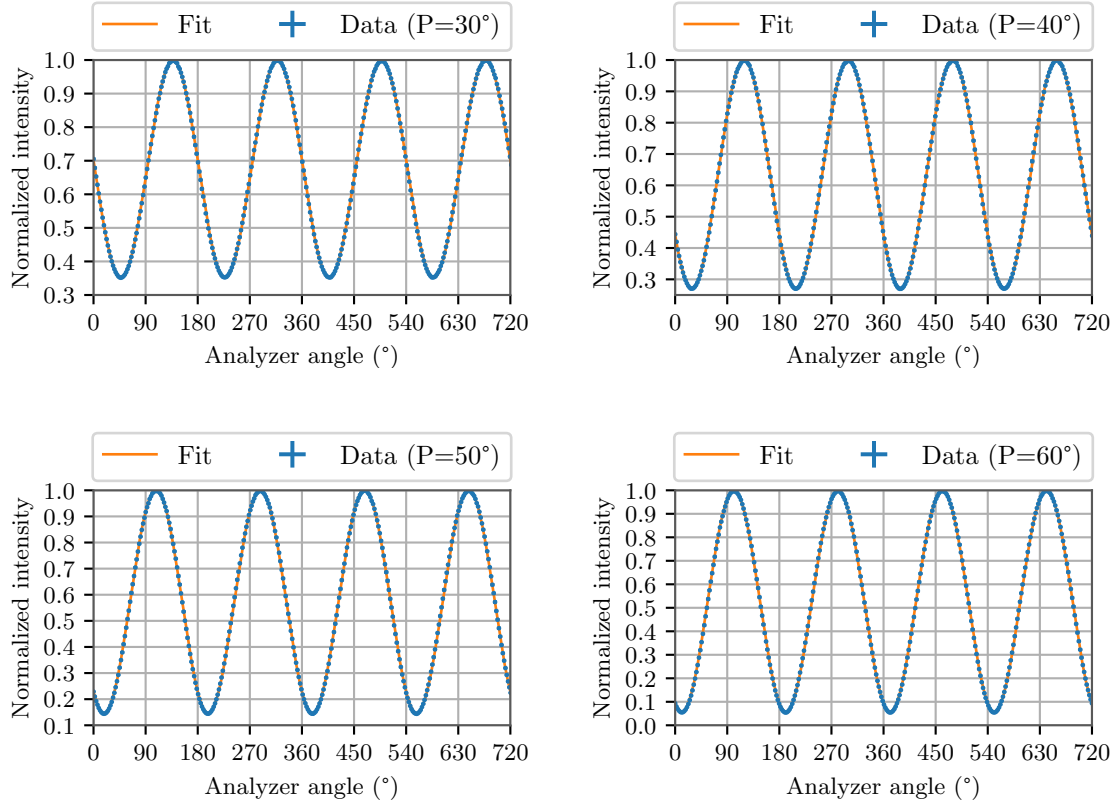


Figure 5.3.1: The intensity curves of the rotating analyzer ellipsometry for the CD sample measured at different polarizer angles P at an incident angle of 60° . The data is fitted with equation 3.5.7.

The angle of incident was changed from 30° to 60° in 5° steps. In figure 5.3.1 a section (0° to 720°) of the measurement with an incident angle of 60° for the polarizer angles of 30° , 40° , 50° and 60° are shown as an example. As the polarizer axis of the rotating analyzer has the same orientation every 180° an intensity curve with maxima and minima which repeat every 180° and 90° apart was expected. If the measurements are compared, it can be seen that the maxima shift towards left the larger the polarizer angle becomes. Also the amplitude of the measurement changes. This behavior continues for larger polarizer angles. This was expected because by changing the polarizer angle the polarization of the light hitting the sample and therefore, the polarization of the light after the reflection is also changing for different polarizer angles. This results in different intensity curves with different amplitudes and maximum positions, too. However, in some measurements it has been noted that the maxima have different intensities. As in the null ellipsometry, this can be traced back to the alignment of the beam and the back reflections. The measurement data was fitted with the equation 3.5.7 in section 3.5.2. From this fit the ellipsometry parameter ψ and Δ can be determined. The ellipsometry parameter for each measurement are listed in table 5.3.1.

If at first the measured values for the same angle of incidence but different polarizer angles are compared with each other, a certain behavior of the ellipsometry parameters ψ and Δ in connection with the polarizer angle becomes apparent. Both parameters change with different polarizer angles and also the effect is different for different incident angles. This effect was expected because when the

polarizer is rotated, the polarization of the light hitting the sample changes and thus ψ and Δ also have different values.

If the measurement had been performed for polarizer angles from 0° to 360° , then the ellipsometry parameters ψ and Δ would repeat every 180° since the polarizer axis has the same orientation every 180° . Thus, a sine-like curve of the ψ and Δ values would be expected when plotted against the polarizer angle. This curve changes for different angles of incidence since not only the polarizer angle has an influence on the polarization but also the angle of incidence. Therefore, the measurements with different incident angles do not allow to expect to show exactly the same behavior with the change of the polarizer. This can be seen very well when comparing the data for the different incident angles.

Table 5.3.1: The two ellipsometry parameters ψ and Δ determined for the CD sample for different polarizer angles at different incident angles.

| Polarizer angle ($^\circ$) | | Incident angle ($^\circ$) | | | | | | |
|------------------------------|-----------------------|-----------------------------|-------------------|-------------------|-------------------|-------------------|-------------------|-------------------|
| | | 30.00 | 35.00 | 40.00 | 45.00 | 50.00 | 55.00 | 60.00 |
| 30 | ψ ($^\circ$) | 342.40 ± 0.01 | 341.33 ± 0.01 | 340.94 ± 0.01 | 340.42 ± 0.01 | 340.47 ± 0.01 | 330.09 ± 0.01 | 329.05 ± 0.01 |
| | Δ ($^\circ$) | 108.6 ± 0.2 | 122.16 ± 0.04 | 129.16 ± 0.03 | 148.39 ± 0.04 | 169.53 ± 0.02 | 172.06 ± 0.01 | 151.51 ± 0.01 |
| 35 | ψ ($^\circ$) | 341.68 ± 0.02 | 340.41 ± 0.01 | 340.22 ± 0.01 | 339.81 ± 0.01 | 340.01 ± 0.01 | 329.66 ± 0.01 | 328.57 ± 0.01 |
| | Δ ($^\circ$) | 106.3 ± 0.3 | 126.12 ± 0.04 | 134.31 ± 0.03 | 152.76 ± 0.04 | 172.55 ± 0.02 | 171.59 ± 0.01 | 150.43 ± 0.01 |
| 40 | ψ ($^\circ$) | 341.09 ± 0.02 | 339.53 ± 0.01 | 339.71 ± 0.01 | 339.54 ± 0.02 | 340.04 ± 0.01 | 329.67 ± 0.01 | 328.54 ± 0.01 |
| | Δ ($^\circ$) | 109.0 ± 0.3 | 132.23 ± 0.04 | 140.91 ± 0.03 | 158.40 ± 0.04 | 176.82 ± 0.02 | 171.06 ± 0.01 | 149.40 ± 0.01 |
| 45 | ψ ($^\circ$) | 340.23 ± 0.03 | 338.48 ± 0.01 | 339.18 ± 0.01 | 339.42 ± 0.04 | 340.41 ± 0.02 | 330.03 ± 0.01 | 328.80 ± 0.01 |
| | Δ ($^\circ$) | 117.7 ± 0.2 | 140.89 ± 0.01 | 149.67 ± 0.03 | 165.54 ± 0.05 | 182.74 ± 0.03 | 170.40 ± 0.01 | 148.21 ± 0.01 |
| 50 | ψ ($^\circ$) | 338.70 ± 0.04 | 336.85 ± 0.01 | 338.26 ± 0.01 | 339.21 ± 0.04 | 340.98 ± 0.02 | 330.75 ± 0.01 | 329.29 ± 0.01 |
| | Δ ($^\circ$) | 130.9 ± 0.1 | 152.26 ± 0.03 | 161.04 ± 0.02 | 175.33 ± 0.06 | 190.50 ± 0.04 | 169.63 ± 0.02 | 146.72 ± 0.02 |
| 55 | ψ ($^\circ$) | 335.65 ± 0.04 | 333.86 ± 0.02 | 336.29 ± 0.02 | 338.29 ± 0.05 | 341.18 ± 0.03 | 331.99 ± 0.01 | 330.23 ± 0.01 |
| | Δ ($^\circ$) | 146.7 ± 0.1 | 165.39 ± 0.03 | 175.24 ± 0.02 | 187.82 ± 0.06 | 201.12 ± 0.06 | 168.75 ± 0.02 | 145.01 ± 0.03 |
| 60 | ψ ($^\circ$) | 330.36 ± 0.04 | 328.89 ± 0.02 | 332.31 ± 0.02 | 335.45 ± 0.06 | 339.80 ± 0.04 | 333.83 ± 0.03 | 331.61 ± 0.02 |
| | Δ ($^\circ$) | 162.51 ± 0.06 | 179.14 ± 0.02 | 190.29 ± 0.02 | 202.4 ± 0.1 | 213.5 ± 0.1 | 167.42 ± 0.02 | 142.86 ± 0.05 |

If now the values for the same polarizer angles but for different incident angles are considered, it can be seen that up to an incidence angle of 50° the values of ψ change only minimally and that ψ gets smaller for higher incident angles. The ellipsometry parameter for the incident angles of 55° and 60° can not be compared to the results of the other incident angles because as mentioned in section 5.2.1 the measurements for these incident angles were redone because of an error in the first measurements. Furthermore, it can be seen in the full scans of 5.2.1 that the measurements slightly differ and so it could be the case that not the same spot on the CD sample was measured. But ψ gets also smaller for higher incident angles, if only the measurements for an incident angle of 55° and 60° were considered. Δ increases up to an angle of incidence of 50° , but for the two measurements for an angle of incidence of 55° and 60° , Δ gets smaller. The change of ψ and Δ again can be explained by the influence of the angle of incidence on the polarization.

Table 5.3.2 lists the refractive indices and layer thicknesses of the polycarbonate layer calculated from ellipsometry parameters for different polarizer angles at different refractive indices. It is clear that there is no particular behavior for different angles of incidence and different polarizer angles. This also was expected since the same values for thickness and refractive index should actually come out for each measurement. As described in section 5.1 a refractive index of $n = 1.5803$ at a wavelength of 635 nm and a thickness of 1.2 mm for the polycarbonate layer were expected. All measured values are within the expected values with their uncertainties. However, it is noticeable that the measurements for incident angles of 55° and 60° give significantly better results which are closer to the expectations and have smaller uncertainties than the other incident angles. This could have its cause in the alignment of the laser beam. The back reflection may have better aligned at this angle of incidence. On the other hand, it could also have to do with that these measurements are redone and that there are slightly alignment changes in comparison to the other measurements.

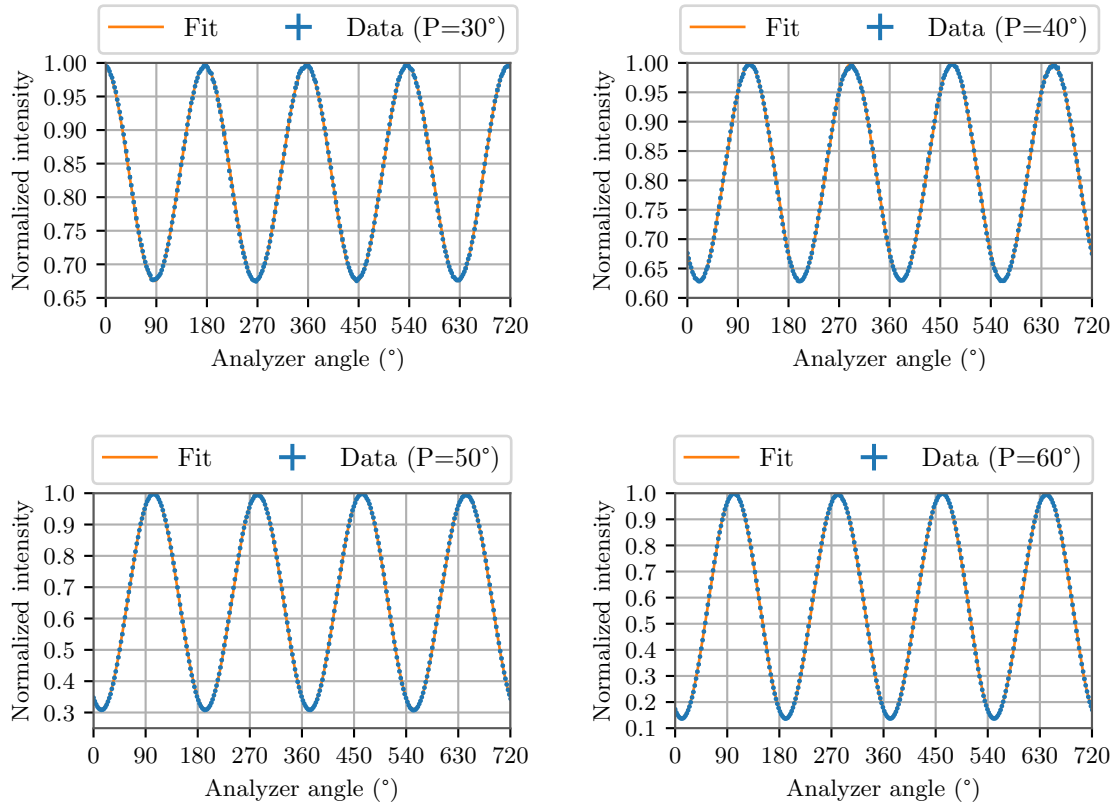
Table 5.3.2: The resulting values for the refractive index n and the thickness d of the polycarbonate layer of the CD sample calculated for different angles of incidence.

| Polarizer angle (°) | | Incident angle (°) | | | | | | |
|---------------------|----------|--------------------|-----------------|-------------------|-------------------|-------------------|---------------------|---------------------|
| | | 30.00 | 35.00 | 40.00 | 45.00 | 50.00 | 55.00 | 60.00 |
| 30 | n | 1.60 ± 0.04 | 1.59 ± 0.06 | 1.60 ± 0.07 | 1.580 ± 0.004 | 1.60 ± 0.07 | 1.581 ± 0.003 | 1.581 ± 0.003 |
| | d (mm) | 1.19 ± 0.04 | 1.19 ± 0.06 | 1.18 ± 0.07 | 1.200 ± 0.003 | 1.19 ± 0.06 | 1.199 ± 0.004 | 1.200 ± 0.003 |
| 35 | n | 1.6 ± 0.1 | 1.60 ± 0.06 | 1.59 ± 0.05 | 1.580 ± 0.002 | 1.580 ± 0.004 | 1.580 ± 0.007 | 1.5802 ± 0.0005 |
| | d (mm) | 1.16 ± 0.09 | 1.19 ± 0.05 | 1.18 ± 0.06 | 1.200 ± 0.002 | 1.200 ± 0.004 | 1.209 ± 0.001 | 1.200 ± 0.001 |
| 40 | n | 1.61 ± 0.07 | 1.59 ± 0.04 | 1.61 ± 0.06 | 1.59 ± 0.02 | 1.60 ± 0.09 | 1.580 ± 0.001 | 1.5798 ± 0.0032 |
| | d (mm) | 1.18 ± 0.07 | 1.19 ± 0.04 | 1.17 ± 0.08 | 1.19 ± 0.05 | 1.19 ± 0.05 | 1.200 ± 0.001 | 1.201 ± 0.004 |
| 45 | n | 1.62 ± 0.09 | 1.59 ± 0.02 | 1.58 ± 0.02 | 1.60 ± 0.08 | 1.59 ± 0.05 | 1.58 ± 0.01 | 1.580 ± 0.001 |
| | d (mm) | 1.16 ± 0.09 | 1.19 ± 0.02 | 1.20 ± 0.01 | 1.18 ± 0.05 | 1.19 ± 0.05 | 1.201 ± 0.008 | 1.2020 ± 0.0010 |
| 50 | n | 1.59 ± 0.02 | 1.61 ± 0.07 | 1.60 ± 0.07 | 1.59 ± 0.04 | 1.59 ± 0.04 | 1.5808 ± 0.0008 | 1.580 ± 0.001 |
| | d (mm) | 1.19 ± 0.01 | 1.17 ± 0.08 | 1.20 ± 0.01 | 1.18 ± 0.06 | 1.19 ± 0.03 | 1.200 ± 0.002 | 1.200 ± 0.001 |
| 55 | n | 1.62 ± 0.09 | 1.6 ± 0.1 | 1.60 ± 0.07 | 1.60 ± 0.07 | 1.59 ± 0.04 | 1.581 ± 0.003 | 1.580 ± 0.002 |
| | d (mm) | 1.17 ± 0.08 | 1.17 ± 0.08 | 1.191 ± 0.040 | 1.18 ± 0.06 | 1.19 ± 0.04 | 1.199 ± 0.004 | 1.200 ± 0.002 |
| 60 | n | 1.6 ± 0.1 | 1.58 ± 0.02 | 1.59 ± 0.04 | 1.60 ± 0.05 | 1.582 ± 0.008 | 1.580 ± 0.004 | 1.579 ± 0.005 |
| | d (mm) | 1.17 ± 0.07 | 1.19 ± 0.05 | 1.19 ± 0.05 | 1.18 ± 0.05 | 1.20 ± 0.01 | 1.200 ± 0.003 | 1.201 ± 0.005 |

In addition, some measurements show stronger variations of intensities at the maxima than other measurements. This could also have an influence on the fit and the ellipsometry parameters and thus also on the calculated refractive index.

5.3.2 Silicon dioxide/ silicon sample

The silicon dioxide (SiO_2) / silicon (Si) sample was measured at an incident angle of 45° and for polarizer angles from 30° to 60° in 5° steps.

**Figure 5.3.2:** A section of the measured intensity curves of the rotating analyzer ellipsometry for the silicon dioxide on silicon sample measured at different polarizer angles P at an incident angle of 45° . The data were fitted with equation 3.5.7.

In figure 5.3.2 a section (0° to 720°) of the rotating analyzer ellipsometry measurement for the sample with polarizer angles at 30° , 40° , 50° and 60° are shown. The measured data were fitted with the equation 3.5.7 from section 5.3. When comparing the data, it can be seen that the change of the polarizer angle has an influence on the amplitude and the position of the maxima of the intensity curve. This was also expected since the change of the polarizer leads to a change of the polarization of the light hitting the sample. Thus, the light passing through the analyzer also has a change in polarization and for this reason the intensity curve changes.

The ellipsometry parameters obtained from the fit are shown in table 5.3.3. The values ψ and Δ change for different polarizer angles. This is in line with the expectations since in the measured data the amplitude and the position of the maxima of the intensity change as described before. This behavior also shows the influence of the polarization changes due to the polarizer angle.

Table 5.3.3: The two ellipsometry parameter ψ and Δ for the silicon dioxide on silicon sample determined for different polarizer angles at an incident angle of 45° .

| Polarizer angle ($^\circ$) | ψ ($^\circ$) | Δ ($^\circ$) |
|------------------------------|---------------------|-----------------------|
| 30 | 325.002 ± 0.002 | 178.691 ± 0.005 |
| 35 | 324.862 ± 0.002 | 174.834 ± 0.003 |
| 40 | 324.745 ± 0.002 | 171.283 ± 0.004 |
| 45 | 324.624 ± 0.003 | 167.893 ± 0.007 |
| 50 | 324.395 ± 0.005 | 164.439 ± 0.010 |
| 55 | 324.124 ± 0.008 | 160.61 ± 0.01 |
| 60 | 323.76 ± 0.01 | 156.23 ± 0.02 |

From the ellipsometry parameters the refractive index and the thickness of the silicon dioxide layer can be determined with the analysis program. The resulting values are listed in table 5.3.4. A refractive index of $n = 1.457$ at a wavelength of 635 nm and a thickness of $d = 285$ nm, as described in section 5.1, was to be expected.

Table 5.3.4: The measured refractive index n and the thickness d of the silicon dioxide layer for different polarizer angles and at an incident angle of 45° .

| Polarizer angle ($^\circ$) | refractive index n | thickness d (nm) |
|------------------------------|----------------------|--------------------|
| 30 | 1.496 ± 0.007 | 272 ± 6 |
| 35 | 1.477 ± 0.006 | 270 ± 6 |
| 40 | 1.477 ± 0.005 | 274 ± 7 |
| 45 | 1.475 ± 0.007 | 273 ± 7 |
| 50 | 1.477 ± 0.005 | 274 ± 7 |
| 55 | 1.476 ± 0.007 | 276 ± 8 |
| 60 | 1.475 ± 0.007 | 277 ± 8 |
| expected value | 1.457 | 285 |

It can be seen that the refractive indices for the measurements are about 0.02 to 0.04 higher than the expected refractive index. Nevertheless, the calculated thickness deviates significantly from the other measurements and has a large uncertainty. The thickness is about 8 nm to 15 nm smaller than expected. This behavior can have several causes. On the one hand, the polarizer angle change can change the orientation of the beam on the sample and the position of back reflections and therefore, the alignment deteriorates. On the other hand, this also can occur by the fit or by the analysis program. Another possibility could be the sample itself because its thickness can vary along the surface of the sample and maybe the measured values could be in the range of this variation.

5.3.3 Bilayer graphene / silicon carbide sample

Analog to the silicon dioxide / silicon sample (cf. section 5.3.2) the bilayer graphene on silicon carbide (SiC) sample was measured for different polarizer angles at an incidence angle of 45° . A section (0° to 720°) of the obtained data for the polarizer angles of 30° , 40° , 50° and 60° is shown in figure 5.3.3. Once again, it can be seen that the intensity curve for the different polarizer angles changes in amplitude and position of the maxima. This also can be explained by the polarization change of the light due to the change of the polarization angle.

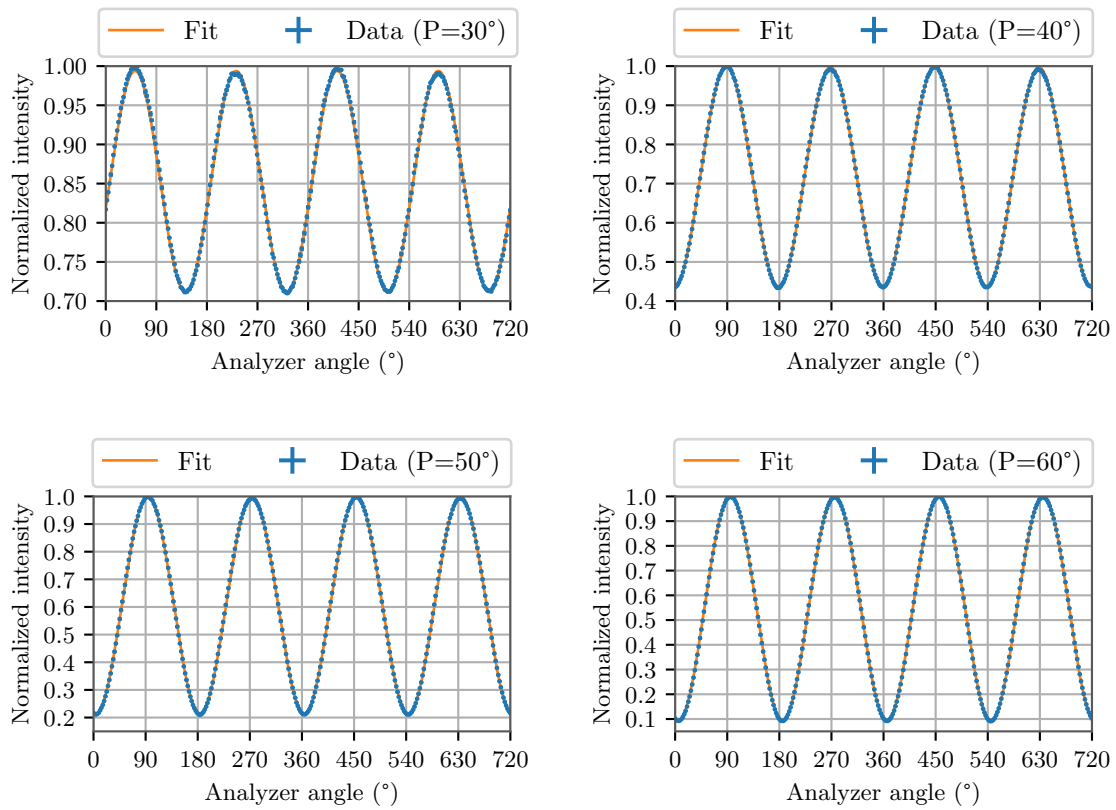


Figure 5.3.3: A section of the intensity curves of the rotating analyzer ellipsometry for the bilayer graphene on silicon carbide sample measured at different polarizer angles P at an incident angle of 45° . The data were fitted with the equation 3.5.7.

The two ellipsometry parameters ψ and Δ were determined by a fit with the equation 3.5.7 from section 5.3. The results are listed in table 5.3.5. As for the other rotating analyzer ellipsometry measurements the two ellipsometry parameters change, if the polarizer angle is changed. This is also caused by the polarization change of the incoming light on the sample and thus also was expected. From the ellipsometry parameters the refractive index n , the extinction coefficient k and the thickness d of the bilayer graphene can be determined. Expected was a refractive index of $n = 2.55 \pm 0.01$, an extinction coefficient of $k = 1.71 \pm 0.01$ and $d = (0.7 \pm 0.4)$ nm for the thickness as described in section 5.1.

The measured parameters are listed in table 5.3.6. For the refractive index n it can be seen that the measured values are about 0.04 larger than the expected value. Furthermore, comparing the values for different polarizer angles, it can be seen that the values of the refractive index n differ only from the third decimal place.

Table 5.3.5: The two ellipsometry parameters ψ and Δ for the bilayer graphene on silicon carbide sample determined for different polarizer angles at an incident angle of 45° .

| Polarizer angle ($^\circ$) | ψ ($^\circ$) | Δ ($^\circ$) |
|------------------------------|---------------------|-----------------------|
| 30 | 330.973 ± 0.003 | 189.259 ± 0.007 |
| 35 | 330.916 ± 0.003 | 185.097 ± 0.007 |
| 40 | 330.911 ± 0.004 | 181.315 ± 0.008 |
| 45 | 330.912 ± 0.005 | 177.57 ± 0.01 |
| 50 | 330.868 ± 0.008 | 173.69 ± 0.01 |
| 55 | 330.84 ± 0.01 | 169.55 ± 0.02 |
| 60 | 330.79 ± 0.02 | 164.26 ± 0.03 |

However, the measured values are not within the uncertainty range of the expected refractive index. This is as well for the case for the measured extinction coefficient. For the extinction coefficient k the expected value is about 0.1 smaller than the measured values. The thickness d , on the other hand, is in the expected range of the expected thickness due to the large uncertainty of the expected thickness but does not include the expected value in its uncertainty range.

Table 5.3.6: The measured refractive index n , the extinction coefficient k and the thickness d of the bilayer graphene for different polarizer angles and at an incident angle of 45° .

| Polarizer angle ($^\circ$) | refractive index n | extinction coefficient k | thickness d |
|------------------------------|----------------------|----------------------------|--------------------|
| 30 | 2.598 ± 0.008 | 1.61 ± 0.02 | (1.1 ± 0.2) nm |
| 35 | 2.599 ± 0.004 | 1.61 ± 0.02 | (1.1 ± 0.2) nm |
| 40 | 2.597 ± 0.007 | 1.61 ± 0.02 | (1.1 ± 0.2) nm |
| 45 | 2.598 ± 0.009 | 1.602 ± 0.008 | (1.1 ± 0.2) nm |
| 50 | 2.595 ± 0.009 | 1.62 ± 0.03 | (1.1 ± 0.2) nm |
| 55 | 2.59 ± 0.02 | 1.62 ± 0.03 | (1.2 ± 0.2) nm |
| 60 | 2.60 ± 0.01 | 1.61 ± 0.02 | (1.1 ± 0.2) nm |
| expected value | 2.55 ± 0.01 | 1.71 ± 0.01 | (0.7 ± 0.4) nm |

These deviations may have to do with the measurement itself. This means that the alignment of the beam is still too inaccurate for this layer thickness and therefore back reflections, for example, have a large influence. This can be as well seen in the measured data because the intensity of the maxima is varying. On the other hand, it can also be due to the evaluation analysis program since in contrast to the two other samples, a third parameter (k) is now taken into account and if one of these parameters shows a general deviation for all polarizer angles, this has an influence on the other parameters.

6 Summary and outlook

The aim of the work was to construct, characterize and commission an ellipsometer. It will be used in the future for the analysis of the photocathode of a photomultiplier to investigate the relationship between the photocathode thickness and the quantum efficiency of the photocathode.

For calibration, the ellipsometer was used to examine three different samples with well-known properties, such as the complex refractive index and the thickness of the layer. The first analyzed sample was a CD with a polycarbonate layer (1.2 mm). The second sample was a silicon dioxide layer with a thickness of 285 nm on a silicon substrate. The third sample consisted of bilayer graphene on silicon carbide and has a thickness of (0.7 ± 0.4) nm. Each of these samples were examined with null ellipsometry and rotating analyzer ellipsometry at an incident angle of 45° . In the case of the CD sample, the measurement was performed also for other angles of incidence.

However, before the samples could be analyzed, the individual optical components of the ellipsometer had to be characterized. The angular displacement between the polarizer axis or the fast axis of the quarter-wave plate and the 0° position of the rotation table were determined and subsequently corrected. The polarization of the laser was also determined using a rotating quarter-wave stokes polarimeter. It was found that the laser emits partially polarized light. Since unpolarized light is required for the measurement, the light was converted to circularly polarized light using a polarizer and quarter-wave plate so that the light appears unpolarized to the polarizer. The last parameter to be characterized was the angle of incidence. After characterization, the angle of incidence had an uncertainty of 0.07° .

Similarly, the subsequent null ellipsometry and rotating analyzer ellipsometry measurements show the same behavior for all samples. In the full scan of the null ellipsometry the intensity pattern repeats every 180° since the polarizer axis and analyzer axis are in the same position after 180° . However, intensity fluctuations can be also detected at the maxima. This can be caused by back reflections and imperfect alignment. The CD measurements shows that the intensity pattern changes for different angles of incidence and that the position of the minimum shifts. This was expected because the change in the angle of incidence changes the change in the polarization of the light after reflection. This also has an influence on the ellipsometry parameters ψ and Δ , whose values also change for different angles of incidence.

In the rotating analyzer ellipsometry also the same behavioral properties between the samples were observed. Here intensity curves were recorded for different polarizer angles. These intensity curves change their amplitude and their position of the maxima for different polarizer angles. Here, too, the ellipsometry parameters ψ and Δ change for different polarizer angles and as in the null ellipsometry also for different incident angles. This is because these two changes have an effect on the polarization of the incident light and the polarization of the reflected light, respectively.

For both types, however, it is noticeable that the calculated values of the complex refractive index and the thickness of the investigated layer for thinner samples deviate relatively more from the expected values than for the thicker samples. Nevertheless, all measured values were in the order of magnitude of the expected values. This deviation may be due to the alignment of the ellipsometer since back

reflection has a significantly greater influence on the measurement of thin samples. The diameter of the laser beam may also be a reason why the thick layers were measured more accurately. However, when comparing both types of ellipsometry, it is noticeable that both produce similar results, except for the bilayer graphene on silicon carbide sample. There the rotating analyzer ellipsometry gets better results for the refractive index n . This could be due to the chosen step size for the minimum scan because if the step size is chosen smaller, the minimum is determined more precisely and so the results should be more precise.

The advantage of the null ellipsometry is that it is easier to determine the ellipsometer parameters ψ and Δ than in the rotating analyzer ellipsometry. But the rotating analyzer ellipsometry is significantly faster than the null ellipsometry.

Since the setup will later be used for photocathode analysis, it needs to be further optimized and analyzed for thinner samples since the photocathode has a thickness of about 20 nm [30]. The setup could be extended with angular adjustable mounts for the optical components to align back reflections even better and to investigate the effect of the better alignment. Also the used analysis program would have to be extended to a four layer model because the photomultiplier has a layer system of air (ambient), glass (first layer), photocathode (second layer) and vacuum (substrate). This extension should be tested with a known four layer system sample. In addition, a photomultiplier tube has a curved surface. This must also be taken into account in the calculation or the photocathode of a photomultiplier with a planar window is examined first. Another problem could be back reflection of the dynode system of the photomultiplier tube. To investigate this influence, a photomultiplier tube without and with dynode system could be investigated to figure out the effect of the back reflections of the dynode system.

All in all, the measurements reflect that the construction and analysis of the ellipsometer was successful and that this ellipsometer can be used for photocathode analysis in the future with a few extensions and additional measurements.

7 Appendix

7.1 Laser intensity

In figure 7.1.1 the laser intensity, as measured by the photodiode¹⁷ without bandpass and 3D-printed box, is plotted against the time. It can be seen that the intensity decreases strongly in the first 100 min and is constant after 120 min. Because of this the laser is turned on for at least two hours before a measurement is started.

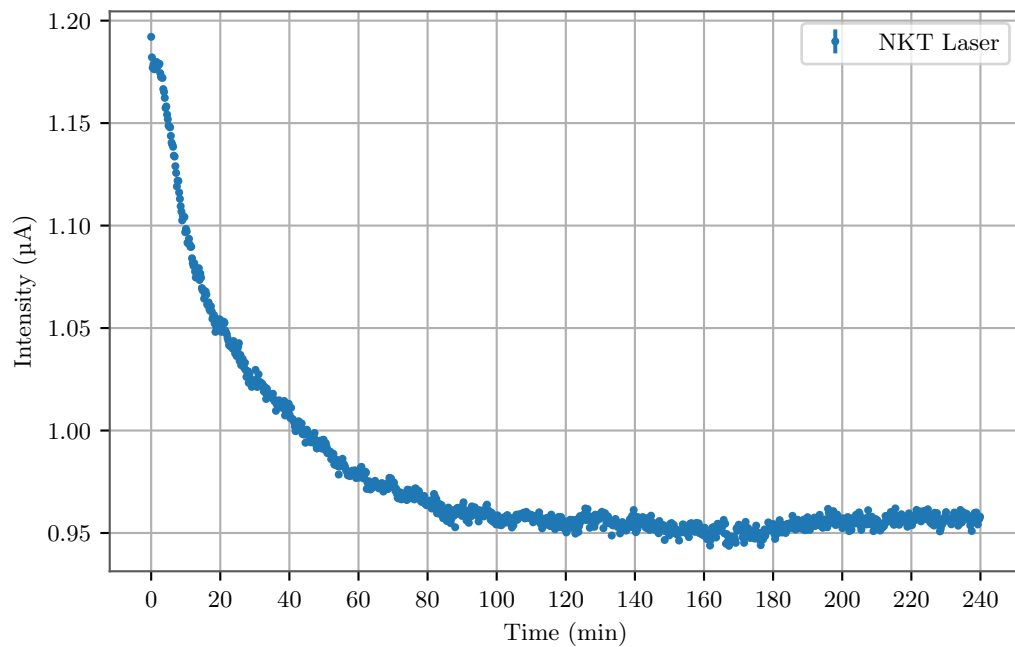


Figure 7.1.1: The laser intensity plotted against the time.

7.2 Laser power density spectrum

Figure 7.2.1 shows the laser power density spectrum of the laser which was used in the measurements at 635 nm as mentioned in chapter 4.1.

¹⁷Newport 818-UV

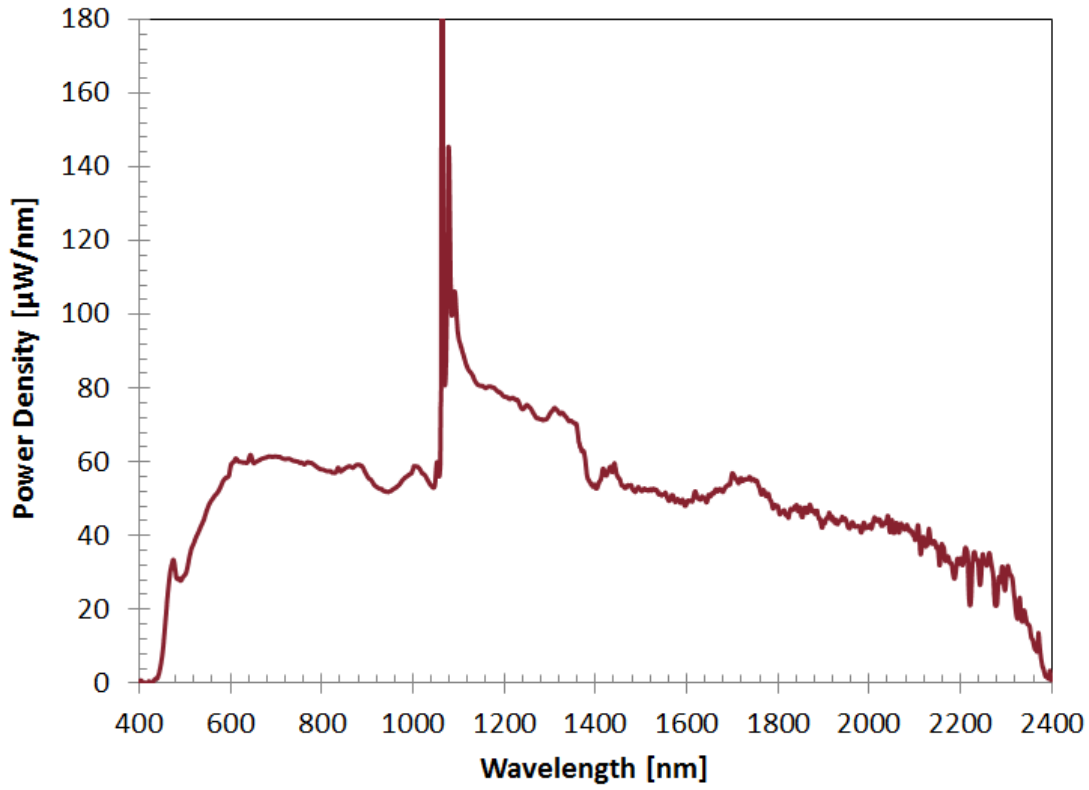


Figure 7.2.1: The power density spectrum of the SuperK Compact Supercontinuum Laser used in the measurements. Figure taken from [31].

7.3 Dielectric function and refractive index

In section 5.1 the dielectric function $\epsilon = \epsilon_1 + i\epsilon_2$ is used to calculate the complex refractive index $N = n + ik$ of silicon crystal and silicon dioxide. In figure 7.3.1 the dielectric function for silicon which was used for the calculation is plotted against the photon energy and the wavelength. In figure 7.3.2 the refractive index n and the extinction coefficient k for silicon for different photon energies and wavelengths are shown.

The data of the dielectric ϵ , the refractive index n and the extinction coefficient k are interpolated linearly to obtain the complex refractive index or rather the real and imaginary part of the dielectric function for a wavelength of 635 nm (1.95 eV) at which all measurements were performed. This is indicated by the red line.

In figure 7.3.3 and 7.3.4 the same plots are shown for the dielectric function ϵ , the refractive index n and the extinction coefficient k of silicon dioxide and in figure 7.3.5 and 7.3.2 for silicon carbide.

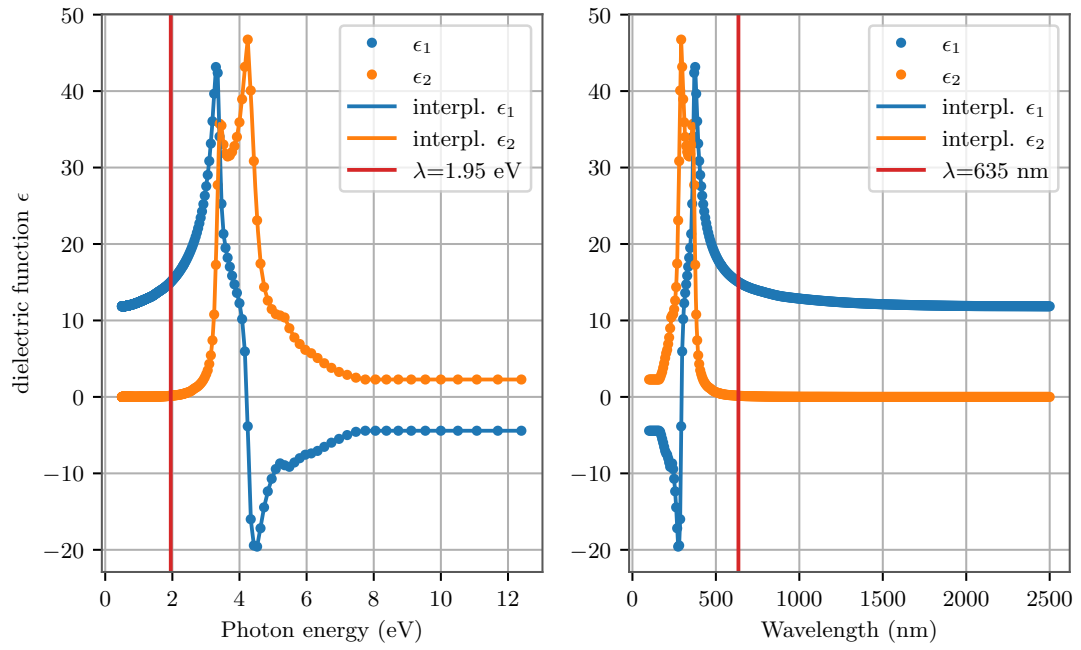


Figure 7.3.1: The dielectric function of crystalline silicon c-Si plotted against the photon energy and the wavelength. Data taken from [28].

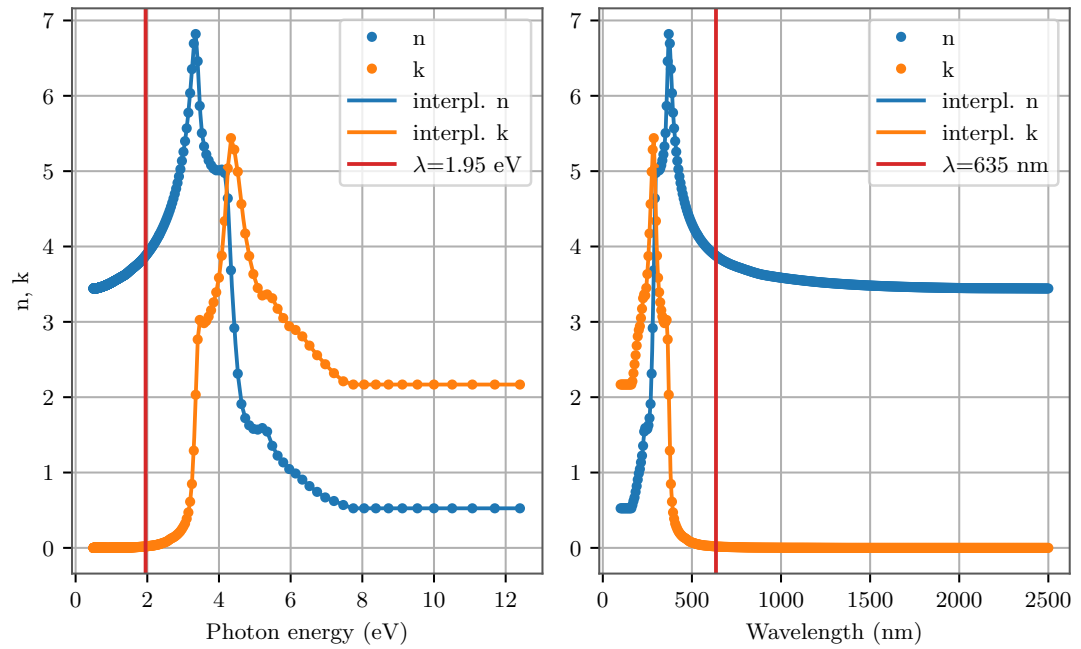


Figure 7.3.2: The refractive index n and the extinction coefficient k of crystalline silicon c-Si for different photon energies and for different wavelengths. Data taken from [28].

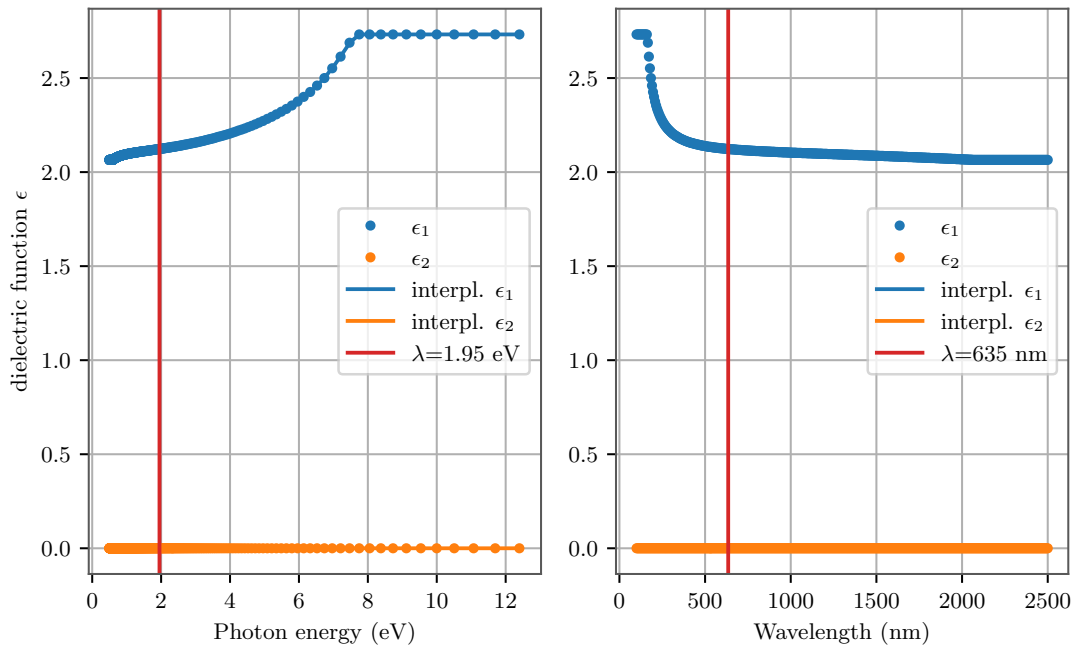


Figure 7.3.3: The dielectric function of silicon dioxide SiO_2 plotted against the photon energy and the wavelength. Data taken from [28].

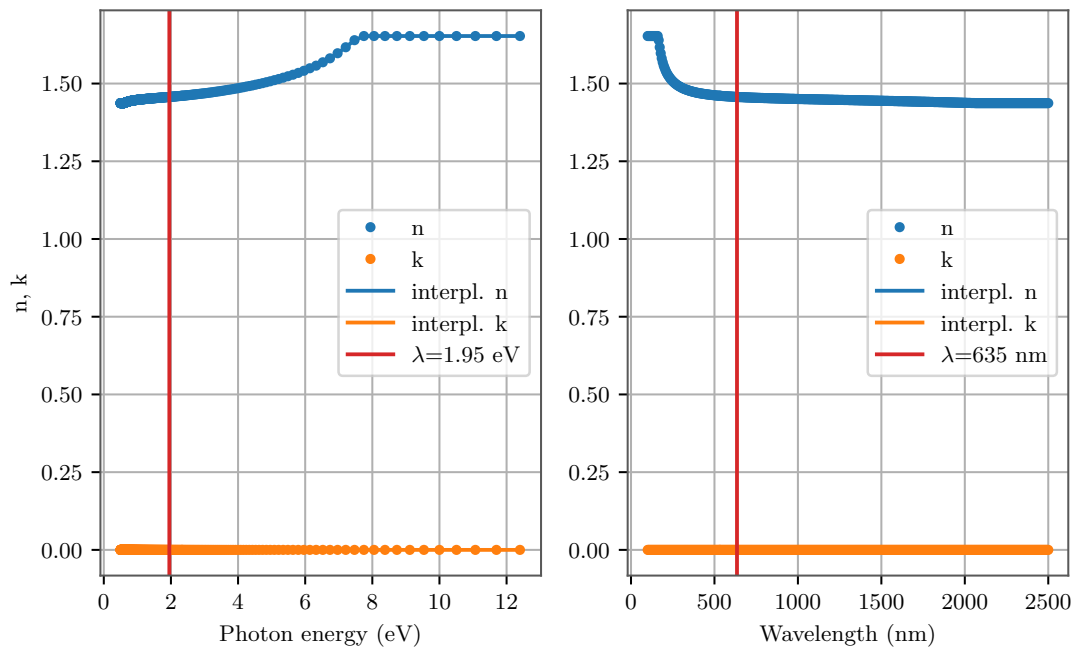


Figure 7.3.4: The refractive index n and the extinction coefficient k of silicon dioxide SiO_2 for different photon energies and for different wavelengths. Data taken from [28].

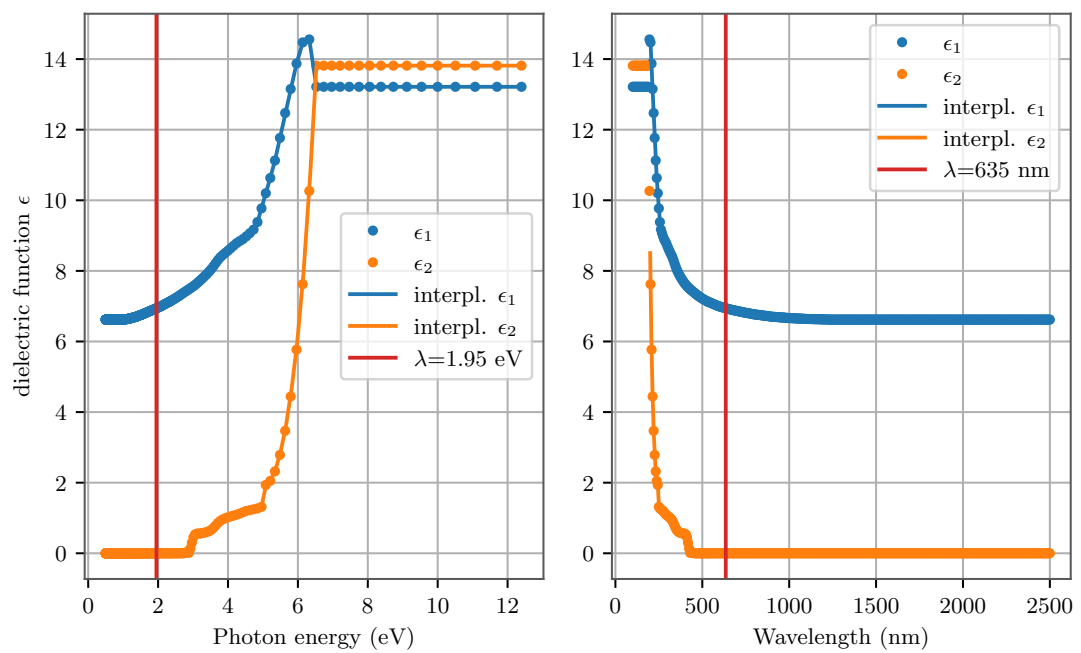


Figure 7.3.5: The dielectric function of silicon carbide SiC plotted against the photon energy and the wavelength. Data taken from [28].

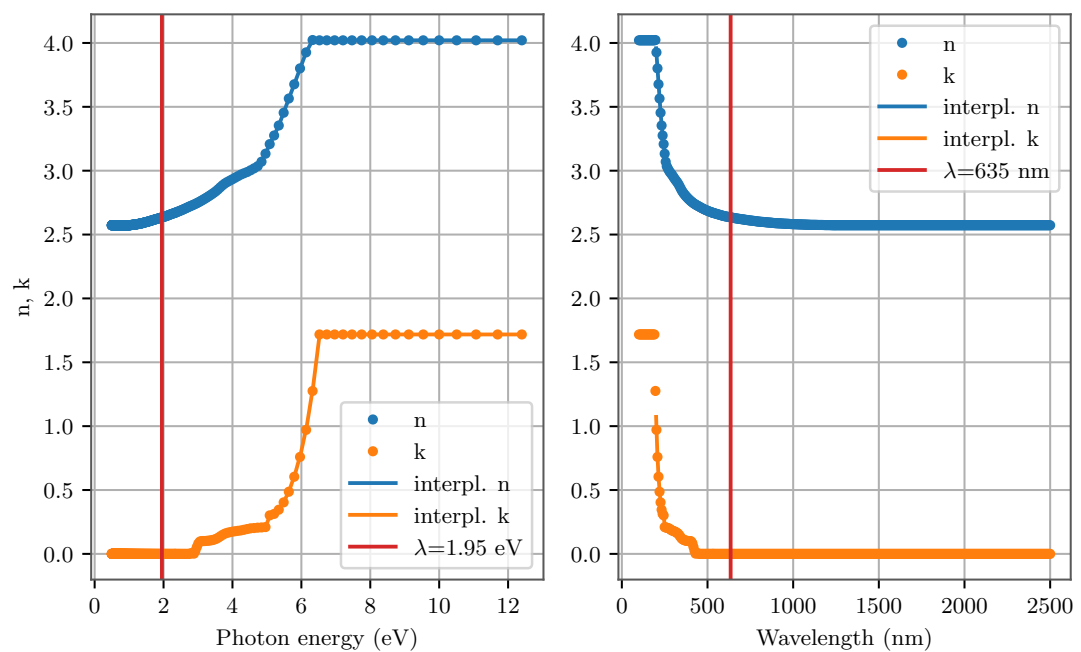


Figure 7.3.6: The refractive index n and the extinction coefficient k of silicon carbide SiC for different photon energies and for different wavelengths. Data taken from [28].

Bibliography

- [1] Claus Grupen. *Einstieg in die Astroteilchenphysik*. Springer Berlin Heidelberg, 2018. DOI: 10.1007/978-3-662-55271-1. URL: <https://doi.org/10.1007/978-3-662-55271-1>.
- [2] IceCube Collaboration. “The IceCube Neutrino Observatory: instrumentation and online systems”. In: *Journal of Instrumentation* 12.03 (Mar. 2017), P03012–P03012. DOI: 10.1088/1748-0221/12/03/p03012. URL: <https://doi.org/10.1088/1748-0221/12/03/p03012>.
- [3] Aya Ishihara. *The IceCube Upgrade – Design and Science Goals*. 2019. arXiv: 1908.09441 [astro-ph.HE].
- [4] M G Aartsen et al. “IceCube-Gen2: the window to the extreme Universe”. In: *Journal of Physics G: Nuclear and Particle Physics* 48.6 (Apr. 2021), p. 060501. DOI: 10.1088/1361-6471/abbd48. URL: <https://doi.org/10.1088/1361-6471/abbd48>.
- [5] Mark Thomson. *Modern Particle Physics*. Cambridge University Press, 2013. DOI: 10.1017/CBO9781139525367.
- [6] M. Aker et al. “Improved Upper Limit on the Neutrino Mass from a Direct Kinematic Method by KATRIN”. In: *Physical Review Letters* 123.22 (Nov. 2019). ISSN: 1079-7114. DOI: 10.1103/physrevlett.123.221802. URL: <http://dx.doi.org/10.1103/PhysRevLett.123.221802>.
- [7] U.F. Katz and Ch. Spiering. “High-energy neutrino astrophysics: Status and perspectives”. In: *Progress in Particle and Nuclear Physics* 67.3 (July 2012), pp. 651–704. DOI: 10.1016/j.ppnp.2011.12.001. URL: <https://doi.org/10.1016/j.ppnp.2011.12.001>.
- [8] M. A. Unland Elorrieta. “Studies on dark rates induced by radioactive decays of the multi-PMT digital optical module for future IceCube extensions”. Dec. 2017. URL: https://www.uni-muenster.de/imperia/md/content/physik_kp/agkappes/abschlussarbeiten/masterarbeiten/1712-ma_munland.pdf.
- [9] J V Jelley. “Cerenkov radiation and its applications”. In: *British Journal of Applied Physics* 6.7 (July 1955), pp. 227–232. DOI: 10.1088/0508-3443/6/7/301. URL: <https://doi.org/10.1088/0508-3443/6/7/301>.
- [10] C. J. Lozano Mariscal et al. “Sensitivity of multi-PMT optical modules in Antarctic ice to supernova neutrinos of MeV energy”. In: *The European Physical Journal C* 81.12 (Dec. 2021). DOI: 10.1140/epjc/s10052-021-09809-y. URL: <https://doi.org/10.1140/epjc/s10052-021-09809-y>.
- [11] Colton Hill et al. *Performance of the D-Egg Optical Sensor for the IceCube Upgrade*. 2021. arXiv: 2108.05353 [physics.ins-det].
- [12] Hamamatsu Photonics K.K. Editorial Committee. *Photomultiplier Tubes. Basics and Applications*. 2007. URL: https://www.hamamatsu.com/resources/pdf/etd/PMT_handbook_v3aE.pdf.

- [13] Photonis. *PHOTOMULTIPLIER TUBES, principles & applications*. Re-edited by S-O Flyckt and Carole Marmonier. Sept. 2002. URL: https://www2.pv.infn.it/~debari/doc/Flyckt_Marmonier.pdf.
- [14] Raffaella Solveig Busse. "Setup and commissioning of a test stand for detailed investigations of quantum efficiency characteristics of photomultiplier tubes, and initial studies for IceCube-Gen2". 2017. URL: https://www.uni-muenster.de/imperia/md/content/physik_kp/agkappes/abschlussarbeiten/masterarbeiten/1703-ma_rbusse.pdf.
- [15] Hiroyuki Fujiwara. *Spectroscopic Ellipsometry, Principles and Applications*. John Wiley & Sons Ltd, 2007.
- [16] H. G. Tompkins and E.A. Irene. *Handbook of Ellipsometry*. Springer-Verlag GmbH & Co. KG, 2005.
- [17] Costel Flueraru et al. "Error Analysis of a Rotating Quarter-Wave Plate Stokes' Polarimeter". In: *IEEE Transactions on Instrumentation and Measurement* 57.4 (2008), pp. 731–735. DOI: 10.1109/TIM.2007.913752.
- [18] STANDA LTD. *8MR170-190 - Motorized Rotary Stages*. URL: https://www.standa.lt/products/catalog/motorised_positioners?item=312&prod=motorized_rotary_stages (visited on 11/05/2021).
- [19] STANDA LTD. *8MR151 - Motorized Rotary Stages*. URL: https://www.standa.lt/products/catalog/motorised_positioners?item=9 (visited on 11/05/2021).
- [20] Physics Instruments (PI) GmbH & Co. KG. *M-060 • M-061 • M-062 Präzisionsdrehtisch*. URL: <https://www.physikinstrumente.de/de/produkte/rotationstische/m-060-m-061-m-062-praezisionsdrehtisch-703100/#specification> (visited on 11/05/2021).
- [21] Physics Instruments (PI) GmbH & Co. KG. *V-610 Kompakter PIMag® Rotationstisch*. URL: <https://www.physikinstrumente.de/de/produkte/rotationstische/v-610-compact-pimag-rotation-stage-412418469/#specification> (visited on 11/05/2021).
- [22] B.Halle Nachfl. GmbH. *Glan-Thompson Polarisationsprismen*. URL: https://www.b-halle.de/produkte/polarisatoren/glan-thompson_polarisationsprismen.html (visited on 12/02/2021).
- [23] Thorlabs. *Mounted Achromatic Wave Plates*. URL: https://www.thorlabs.com/newgrouppage9.cfm?objectgroup_id=854 (visited on 12/02/2021).
- [24] Thorlabs. *Optics Handling and Care Tutorial*. URL: https://www.thorlabs.com/newgrouppage9.cfm?objectgroup_id=9025 (visited on 12/02/2021).
- [25] John A Cope. "The physics of the compact disc". In: 28.1 (Jan. 1993), pp. 15–21. DOI: 10.1088/0031-9120/28/1/003. URL: <https://doi.org/10.1088/0031-9120/28/1/003>.
- [26] N. Sultanova, S. Kasarova, and I. Nikolov. "Dispersion Properties of Optical Polymers". In: *Acta Physica Polonica A* 116.4 (Oct. 2009), pp. 585–587. DOI: 10.12693/aphyspola.116.585. URL: <https://doi.org/10.12693/aphyspola.116.585>.
- [27] Aleksandar D. Rakić. "Algorithm for the determination of intrinsic optical constants of metal films: application to aluminum". In: *Applied Optics* 34.22 (Aug. 1995), p. 4755. DOI: 10.1364/ao.34.004755. URL: <https://doi.org/10.1364/ao.34.004755>.
- [28] U. Wurstbauer. *private communication*.

- [29] Efraín Ochoa-Martínez et al. “Determination of a refractive index and an extinction coefficient of standard production of CVD-graphene”. In: *Nanoscale* 7.4 (2015), pp. 1491–1500. DOI: 10.1039/c4nr06119e. URL: <https://doi.org/10.1039/c4nr06119e>.
- [30] A. G. Wright. *The Photomultiplier Handbook*. Oxford University Press, Aug. 2017. DOI: 10.1093/oso/9780199565092.001.0001. URL: <https://doi.org/10.1093/oso/9780199565092.001.0001>.
- [31] NKT Photonics A/S. *SUPERK COMPACT SUPERCONTINUUM LASERS*. URL: <https://www.nktpotonics.com/lasers-fibers/product/superk-compact-supercontinuum-lasers/> (visited on 11/05/2021).

Acknowledgement

I would like to thank

- Professor Dr. Alexander Kappes for the opportunity to write my master thesis in his working group and for the friendly cooperation within it.
- Professor Dr. Christian Weinheimer for the second correction of my master thesis and the helpful information for the construction of an ellipsometer.
- Martin Unland, Markus Dittmer und Dr. Lew Classen for answering my questions and for proofreading my master thesis.
- Lukas Wahmes for the design of the ellipsometer and the help with the construction of it.
- Daniel Bonaventura for the production of possible samples.
- Fausto Frisenna for writing the analysis program.
- Professor Dr. Ursula Wurstbauer and Margaux Lassauniere for providing the measured samples and their properties.
- the whole working group for the good working atmosphere and the nice time in the laboratory and office.
- David Koke for the coffee breaks and Mathias Kuschick for the walks around the institute.
- my mother and my boyfriend for additional proofreading.